



Contents lists available at ScienceDirect

## Materials &amp; Design

journal homepage: [www.elsevier.com/locate/matdes](http://www.elsevier.com/locate/matdes)

# Multi-objective shape optimization of large strain 3D helical structures for mechanical metamaterials

Guglielmo Cimolai, Iman Dayyani\*, Qing Qin

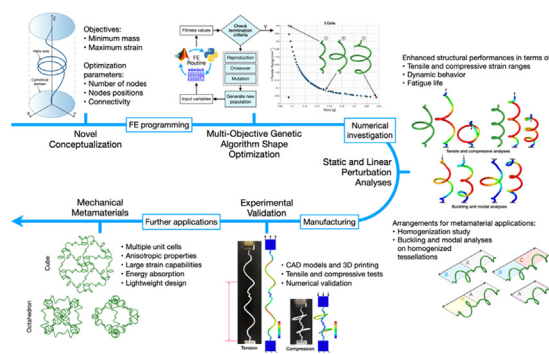
Centre for Structures, Assembly and Intelligent Automation, Cranfield University, MK43 0AL, UK



## HIGHLIGHTS

- A novel methodology of designing 1D mechanical metamaterials composed of periodically repeating helical structures is proposed.
- Genetic algorithm shape optimized structures are compared with conventional springs, demonstrating their advantage over traditional design.
- Optimized structures are manufactured and experimentally tested to validate the proposed numerical methodology, achieving mass reduction.

## GRAPHICAL ABSTRACT



## ARTICLE INFO

## Article history:

Received 30 November 2021  
 Revised 23 January 2022  
 Accepted 30 January 2022  
 Available online 18 February 2022

## Keywords:

3D Helical Structures  
 Multi-objective Shape Optimization  
 Finite Element Analysis (FEA)  
 Large Strain  
 Linear Perturbation Analysis  
 Mechanical Metamaterials

## ABSTRACT

The need for mechanical metamaterials with large strain range and lightweight properties are evidenced to engineering applications. In this regard, novel helical structures are proposed as suitable unit cell's components of mechanical metamaterials. Three-dimensional helical structures composed of varying coil numbers, defined in a cylindrical spatial domain are shape optimized through genetic algorithm in a finite element script for conflicting objectives of minimum mass and maximum tensile range. The superior performance of the shape optimized helical structure is highlighted in terms of structural rigidity, large deformation capability, buckling and vibrational modal analysis in compare to equivalent coil springs of identical weight and comparable domain. Deformation mechanism is analyzed carefully to justify the improved performances of proposed structure. Tensile and compressive experimental analysis are undertaken to validate the enhanced strain ranges. One dimensional metamaterials implementations with various tessellation arrangements are simulated. Results show that the proposed design can effectively generate lightweight substitutes of metamaterials unit cells ligaments to improve the strain range performance. Planar and lattice metamaterial concepts employing shape optimized helical structure are illustrated to demonstrate the possibilities of promoting lightweight structural integrities in the design of mechanical metamaterials.

© 2022 Cranfield University. Published by Elsevier Ltd. This is an open access article under the CC BY license (<http://creativecommons.org/licenses/by/4.0/>).

## 1. Introduction

Structural engineering continuously aims to reduce the weight of its products while improving the mechanical performances. Hel-

ical structures are frequently used in many mechanical applications, such as suspension systems, shock absorbers and large strain elements.

The study of coil spring modelling, mainly focused on conventional springs, has gone through a long process starting from early works of Wittrick [1], who derived governing differential equations using Timoshenko and Euler-Bernoulli beam theories. Mottershead

\* Corresponding author.

E-mail address: [I.Dayyani@cranfield.ac.uk](mailto:I.Dayyani@cranfield.ac.uk) (I. Dayyani).

[2] proposed a FE model for dynamic analysis of rods. In recent years, FE models for curved beam elements have been studied. Taktak et al. [3] proposed a two-node FE model, suitable for isotropic helical structures, considering shear strain effects. Zhang et al. [4] implemented a similar model based on Euler-Bernoulli theory for dynamic analysis of slender beams, and Meier et al. [5] developed a FE model for curved beams based on Kirchhoff theory. Little work has been done on non-conventional coil springs of variable pitch and radius. Chaudury and Datta [6] studied prismatic structures of non-circular coil shape by analytical and FE methods and compared their modelling with straight beam elements. Zhang et al. [7] proposed an analytical dynamic modelling of non-conventional helical elements based on Euler-Bernoulli beam theory. Performances of helical structures have been discussed regarding their buckling and vibrational modal behavior, their deformation capabilities, and their energy absorption characteristics. Becker and Cleghorn [8] first studied buckling behavior of coil springs analytically, based on early works of Haringx, and proposed design charts. De Crescenzo and Salvini [9] proposed a 2D buckling model with lumped stiffness applicable to conventional and non-conventional springs. Chaudury and Datta [6] obtained analytical solutions for the prediction of buckling phenomena in non-conventional springs. Initial work on dynamic behavior has been done by Yildirim [10], who found approximate solutions for predicting vibration frequencies of helical springs. Zhou et al. [11] studied dynamic failure of metro vehicle springs finding a clear influence of resonance phenomena on mechanical failure. Sun et al. [12] analyzed dynamic stiffness characteristics of automotive suspension systems with superposition method and shock wave theory respectively, finding a change in stiffness due to frequency excitation. Dai et al. [13] have proposed different methodologies, namely lumped masses, a Timoshenko beam, and a spring element, to simulate the dynamic behavior and stiffness changes of suspension systems in multi-body vehicle dynamic simulations.

Different optimization approaches exist for improving structural performances from the lightweight perspective, topology and shape optimization among others. In particular, shape optimization aims to improve performances of a given structure, by directly acting on parameters defining its geometry, for achieving the desired objectives [14]. Related to spring design problems, numerous studies have been conducted on the optimization of helical springs, mainly directed to minimizing the weight, maximizing the stiffness or the resonance frequencies. First study by Yokota et al. [15] formulated an optimal mass problem for a helical spring subject to constraints such as allowable shear stress, winding number and wire sectional diameter, into a nonlinear integer programming problem solved with GA. Xiao et al. [16] solved the optimal mass problem employing Particle Swarm Optimization algorithm, giving shear stress, allowable deflection, first modal frequency, fatigue resistance, buckling, conditions of coil non-touch and desired strength as constraints. Taktak et al. [17] proposed a numerical model incorporating dynamic parameters as constraints, and solved it for the minimum mass and the maximum first natural frequency of the spring, respectively, by testing different numerical methods, such as Pattern Search, Interior Point, Active Set and GA. Zhan et al. [18] optimized the design of composite helical structures through GA and Response Surface models. Main limits of these works are the use of single objective optimizations, which cannot guarantee the satisfaction of other conflicting objectives, and a generally unspecified relation between domain and codomain of optimization. Recent works focused on multi-objective optimization of helical structures by means of GA method have been proposed. Zebdi et al. [19] and Ratle et al. [20] used well-known NSGA-II Algorithm for finding Pareto Fronts of conflicting objectives, such as minimum mass and maximum stiffness, verifying their findings with experimental testing. Bai et al.

[21] investigated seven different GAs to determine the best practice when maximizing compressive stiffness and minimizing weight of composite helical structures with MOEA-D and NSGA-II ranked first and third respectively. The spring optimization studies previously discussed aimed to improve performances of conventional coils springs by acting on hyperparameters such as the number of active coils, the values of pitch and external radius or the wire thickness. An overall uniformity of the spring geometry was therefore maintained. Innovative shape optimization approaches have been implemented on planar and three-dimensional truss structures by Lim et al. [22], Jha and Dayyani [23], and Ermakova and Dayyani [24]. Lim et al. [22] proposed topology and shape optimization of a three-dimensional truss structure as a substitute of conventional beams. Jha and Dayyani [23] optimized the Fish-Cells metamaterial by acting on nodes defined along the unit cell shape. Ermakova and Dayyani [24] optimized the shape of a corrugated skin for morphing applications, again selecting nodes in space for the structural connections. These works implemented GA multi-objective optimizations for finding tradeoffs between conflicting objectives and used custom MATLAB routines for performing FE analyses, then validating their code with ABAQUS and experimental testing. However, they were limited to frame structures which can be solved directly by computing the stiffness matrix of the system in MATLAB.

Little work has been done on general approaches for the optimization of non-conventional helical structures. Current need is to have a reliable strategy to design optimized helical structures for variable number of coils, with improved compliance and large strain capabilities. In this paper a novel design of three-dimensional helical structures with variable pitches and radiuses defined in a cylindrical spatial domain is proposed. Shape optimization is performed using a multi-objective GA method for conflicting objectives of minimum mass and maximum yielding strain. Performances of optimized structures are compared with equal-mass conventional coil springs of constant pitch and radius laying in the same spatial domain. Their advantages in light of metamaterial applications are discussed and validated by experimental analysis.

## 2. Problem formulation

A novel methodology for defining the shape of three-dimensional helical structures composed of varying coil numbers is proposed as shown in Fig. 1. Helical structures are discretized through interpolation nodes expressed in cylindrical coordinates  $\{\rho, \theta, z\}$ , with equal distance on the base circumference. These interpolation nodes define the mesh of the structure and can occupy any position in a given cylindrical domain. They are connected by three-dimensional frame elements which bear extensional, bending, and torsional loads to generate the continuous curved helix wire. The  $\rho$  and  $z$  coordinates of these nodes are the controlled design variables. Helical structures are optimized for the position of such nodes, assuming a wire cross-section of circular profile with constant radius.

As to reduce dimensionality of the problem,  $\rho$  and  $z$  coordinates of successive mesh nodes are obtained by evaluation of quota and radius functions, as highlighted in Fig. 1(a, b). Controller nodes are defined, classified as basics or non-basics. Basic Nodes (BNs) are fixed in the design space and used for defining end conditions of helical structures. Non-Basic Nodes (NBNs) constitute the design variables and can be positioned inside the given design space. Controller BNs and NBNs (controller design variables) determine  $\rho$  and  $z$  coordinates of all the controlled mesh nodes (controlled design variables), via interpolation and evaluation of quota and radius functions. The multi-objective optimization problem formulated

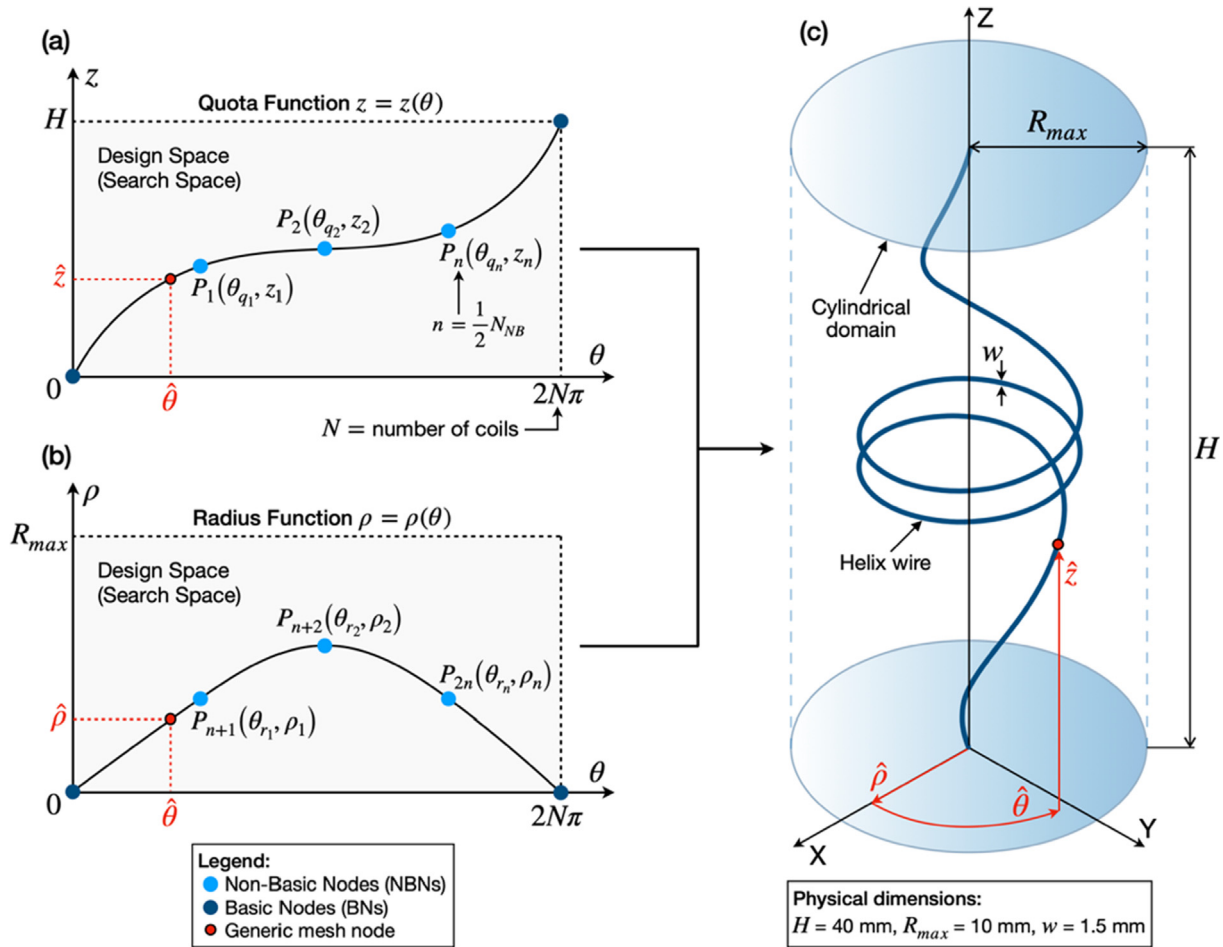


**Fig. 1.** Novel conceptualization of arbitrary 3D helical shape and corresponding dimensions, relationships between fixed nodes (dark blue), optimization nodes (light blue), and mesh nodes (red). (a) Quota function  $z(\theta)$ , (b) radius function  $\rho(\theta)$ , (c) cylindrical domain.

seeks to increase performances of helical structures by optimizing the conflicting objectives of minimum structural weight and maximum tensile range. Different numbers of coils and different numbers of NBNs for a given coil number are investigated in the selected cylindrical domain represented in Fig. 1(c). Optimization is performed in MATLAB using Genetic Algorithm (GA) toolbox due to its suitedness for multi-objective optimization problems. Finite Element (FE) analyses are performed by ABAQUS for evaluating fitness values of each individual in the population. A 3D FE script based on thin beam elements with cubic shape functions is, therefore, written for the implementation of the optimization procedure.

### 2.1. Helical structure parametrization

Given BNs positions, the helical structure's geometry is parametrized by means of controller NBNs, whose coordinates are collected in the vector  $\vec{x}$ , defined in Eq. (1):

$$\vec{x} = \{ \vec{q}, \vec{r} \}$$

$$\vec{q} = \left\{ \theta_{q_1}, z_1, \theta_{q_2}, z_2, \dots, \theta_{q_{\frac{1}{2}N_{NB}}}, z_{\frac{1}{2}N_{NB}} \right\}$$

$$\vec{r} = \left\{ \theta_{r_1}, \rho_1, \theta_{r_2}, \rho_2, \dots, \theta_{r_{\frac{1}{2}N_{NB}}}, \rho_{\frac{1}{2}N_{NB}} \right\}$$
(1)

The vector of parameters  $\vec{x}$  is subdivided into two parts: the quota vector  $\vec{q}$  encoding  $z$ -coordinate variability of controlled mesh nodes, and the radius vector  $\vec{r}$  encoding  $\rho$ -coordinate variability. It has a length of  $2N_{NB}$ , where  $N_{NB}$  is the overall number of NBNs defined. Each element  $x_i$  in  $\vec{x}$  defines each controller node coordinate. The components of  $\vec{q}$  represent nodal coordinates in the  $z - \theta$  plane, those of  $\vec{r}$  represent nodal coordinates in the  $\rho - \theta$  plane, as highlighted in Fig. 1(a, b). Interpolation of BNs and NBNs is performed employing piecewise cubic polynomials to avoid overshoots guaranteeing smoothness. The interpolated functions are evaluated every  $2\pi/N_m$  rad, where  $N_m$  is the number of mesh nodes per coil set equal to  $N_m = 128$  after a mesh sensitivity analysis, thus providing best tradeoff between high accuracy of results and low computational time. The suitable number of NBNs is a problem variable and different values are tested for fixed coil numbers to understand relative influences. NBNs coordinates in the  $z - \theta$  and  $\rho - \theta$  planes are constrained between selected bounds to ensure the helical structure remains inside the given cylindrical spatial domain, shown in Fig. 1(c).

### 2.2. Optimization approaches

The multi-objective optimization problem outlined in the introduction of this section can be formalized as in Eq. (2):

$$\text{minimize } F(\vec{x}) = [f_1(\vec{x}), f_2(\vec{x})] = [m, 1/u_y]$$
(2)

where the first objective  $m$  represents the total mass of the helical structure, while  $u_y$  in the second objective refers to the tensile displacement at yielding.

The modern trend for solving multi-objective optimization problems is by using metaheuristics approaches such as Genetic Algorithms, Particle Swarm Optimization, Simulated Annealing and others [25], which implement non-dominated ranking and selection strategies to move a population of solutions towards the Pareto Front of the problem. In the present paper MATLAB gamultiobj() solver has been selected for easiness of implementation and for its efficiency in shape optimization-related problems [21], which is based on an elitist version of well-known NSGA-II. Due to the stochastic nature of GA optimization and the consequent significant spread of solutions, choices of different parameters are to be made for assuring correct convergence. In the studied implementation MATLAB default hyperparameters were used [26], except for population size  $P$  and crossover fraction  $c_f$ . A crossover fraction  $c_f = 0.3$  has been selected to minimize deviation for each objective and mean value of optimization results, as demonstrated by Dayyani and Friswell [27] who solved a similar problem. After testing population sizes of  $P = [50, 100, 200, 400]$  individuals, a population of  $P = 200$  was selected finding a tradeoff between computational time and optimization effectiveness. Vectorization of the fitness function has been activated to parallelize the GA scheme thus evaluating the fitness of the whole population at once, as to improve computational performances.

Optimization runs have been performed for one to five coils with consistent preliminary studies carried out varying the number of NBNs utilized for a fixed number of coils, with two to twelve NBNs (equally subdivided in the two functions) considered for each case. After parametric studies performed for different coils, six NBNs for one and two coil optimizations and eight NBNs for three to five coil optimizations were then selected as they maximized performances assuring shape convergence of the obtained designs. Cylindrical domain sizes were fixed as  $H = 40 \text{ mm}$  and  $R_{\max} = 10 \text{ mm}$ . The wire circular cross-section  $w$  is maintained constant with diameter equal to  $1.5 \text{ mm}$ .

Feasibility of structures in the design space is enforced through the definition of spatial bounds and constraints  $G_i$ , collected in Table 1. Constraint  $G_1$  sets conditions on the extreme bounds of the quota function, permitting avoiding excessive mesh distortions. Constraint  $G_2$  defines two envelopes which filter out infeasible designs with interpenetrated coils. Constraint  $G_3$  is a condition on the derivative of the quota function, which guarantees its monotony. Constraint  $G_4$  sets conditions on the extreme bounds of the radius function, with limits on the minimum and maximum radius values to avoid coil interpenetrations and cylindrical domain exit. Constraints  $G_5$  and  $G_6$  define initial derivative values at two ends of both functions for avoiding excessive mesh twisting, which lead to inaccurate solutions. Numerical values of upper and lower bounds and envelope constraints for the performed opti-

mizations, as well as corresponding applied tensile displacements, are reported in Table 2. Applied displacements for each case have been selected after preliminary runs to ensure good coverage of the Pareto Fronts especially in the most central region. Moreover, excessive displacement values can lead to severe stretching deformations of low mass geometries which can cause job abortions and prematurely stopping the optimization run, due to the impossibility of computing fitness values.

### 2.3. Finite element script formulation

For computing individual fitness values through the integration of FE analyses inside the iterative optimization procedure, a set of MATLAB scripts has been developed and implemented in the GA fitness function workflow. FE solving capabilities of commercial ABAQUS/Standard software allow for a large iteration rate necessary in GA for convergence. Communication between software is enabled by data file exchange through Python scripting. A flowchart of the developed code is represented in Fig. 2.

Preprocessing is performed in MATLAB through elaborations of user-defined options and GA variables. The chromosome  $\vec{x} = \{\vec{q}, \vec{r}\}$  is inputted in the fitness routine and used for the interpolation of quota and radius functions and generation of each helical structure geometry. Data are then imported in ABAQUS through the writing of input files, singularly for each individual in each generation, which completely define the requested FEA. After the analysis is submitted and the output database file is created, requested field and history values are accessed by Python scripts and re-imported in MATLAB to be post-processed. Vectorization of gamultiobj() fitness function allows for the contemporary submission of multiple FE analyses, thus permitting to parallelize all fitness evaluations in a generation. The process of ranked scoring and reproduction is iteratively performed until a termination criteria, related to a specified tolerance on spread of solutions, is met [28]. Steps 8 and 9 in Fig. 2 are intended to be repeated until satisfaction of termination criteria.

For the model definition of individual helical structures three-node quadratic beam elements B32 have been used, which represent Timoshenko shear flexible beams. A seed of 64 elements per coil as per Section 2.1, has been selected. Circular profile cross-section of constant radius has been defined. Although a full optimization of both geometry and material properties may be suitable for best results, this paper is focused on geometric parameters only. As such, Nylon PA-2200 base material is considered, modelled through a linear elastic-plastic constitutive behavior with properties extracted from literature and reported in Table 3 [29].

A standard static analysis has been defined with 1s time period and request of 100 evenly spaced intervals for both field and history outputs, achieving clear resolution of the output time evolution maintaining computational time low. Nonlinear geometry has been activated for dealing with large deformations. One end of the helical structure has been encastred, while the other end has been given an imposed displacement in the positive longitudinal z-direction with displacement values reported in Table 2. Whole model Von Mises stress field values and load point displacement values have been requested at all time frames for the individuation of the elastic tensile range of the helical structure, which marks the change from the purely elastic reversible behavior to the unreversible one characterized by permanent plastic deformations involved in the deformation process.

The mass of the structure is directly extracted from the model's data in the database file and is obtained from the summation of individual masses of beam elements,  $f_1(\vec{x}) = \sum_e (\rho A \int dl)_e$ , where  $\rho$  is material density,  $A$  is wire's cross sectional area and  $\int dl$  repre-

**Table 1**  
Analytical relations of optimization bounds and spatial constraints.

Constraint	Definition	Description
$G_1$	$\vec{q}_{\min} \leq \vec{q} \leq \vec{q}_{\max}$	Constraint nodes within spatial domain avoiding mesh distortions (upper and lower bounds).
$G_4$	$\vec{r}_{\min} \leq \vec{r} \leq \vec{r}_{\max}$	
$G_2$	$q(\theta) \geq \alpha\theta, q(\theta) \leq \alpha\theta + \beta$	Filter unfeasible designs with interpenetrated coils and provide end conditions.
$G_3$	$\frac{dq(\theta)}{d\theta} \geq \alpha$	
$G_5$	$\frac{dq(\theta)}{d\theta}  _{\theta=0, 2N\pi} = \alpha$	Avoid excessive mesh twisting at the two ends of the helical structure.
$G_6$	$\frac{dr(\theta)}{d\theta}  _{\theta=0} = 1, \frac{dr(\theta)}{d\theta}  _{\theta=2N\pi} = -1$	



**Table 2**  
Numerical values of optimization bounds and spatial constraints for the five considered cases.

Coil number ( $\theta$ range)	Parameters $\alpha$ [ $\frac{mrad}{rad}$ ] and $\beta$ [mm]	Lower and upper bounds			NBNs used	Applied displacement [mm]
		$[\theta_{min}, \theta_{max}]$ [rad]	$[z_{min}, z_{max}]$ [mm]	$[\rho_{min}, \rho_{max}]$ [mm]		
1 ( $\theta \in [0, 2\pi]$ )	$\alpha = \frac{5}{2\pi}, \beta = 35$	$[\frac{1.5\pi}{4}, \frac{6.5\pi}{4}]$	[0, 40] subject to constraints $G_2, G_3$	[2.5, 10]	6	20
2 ( $\theta \in [0, 4\pi]$ )	$\alpha = \frac{2.5}{4\pi}, \beta = 32.5$	$[\frac{3\pi}{4}, \frac{13\pi}{4}]$			6	20
3 ( $\theta \in [0, 6\pi]$ )	$\alpha = \frac{10}{6\pi}, \beta = 30$	$[\frac{3\pi}{4}, \frac{21\pi}{4}]$			8	25
4 ( $\theta \in [0, 8\pi]$ )	$\alpha = \frac{12.5}{8\pi}, \beta = 27.5$	$[\frac{3\pi}{4}, \frac{29\pi}{4}]$			8	30
5 ( $\theta \in [0, 10\pi]$ )	$\alpha = \frac{15}{10\pi}, \beta = 25$	$[\frac{3\pi}{4}, \frac{37\pi}{4}]$			8	35

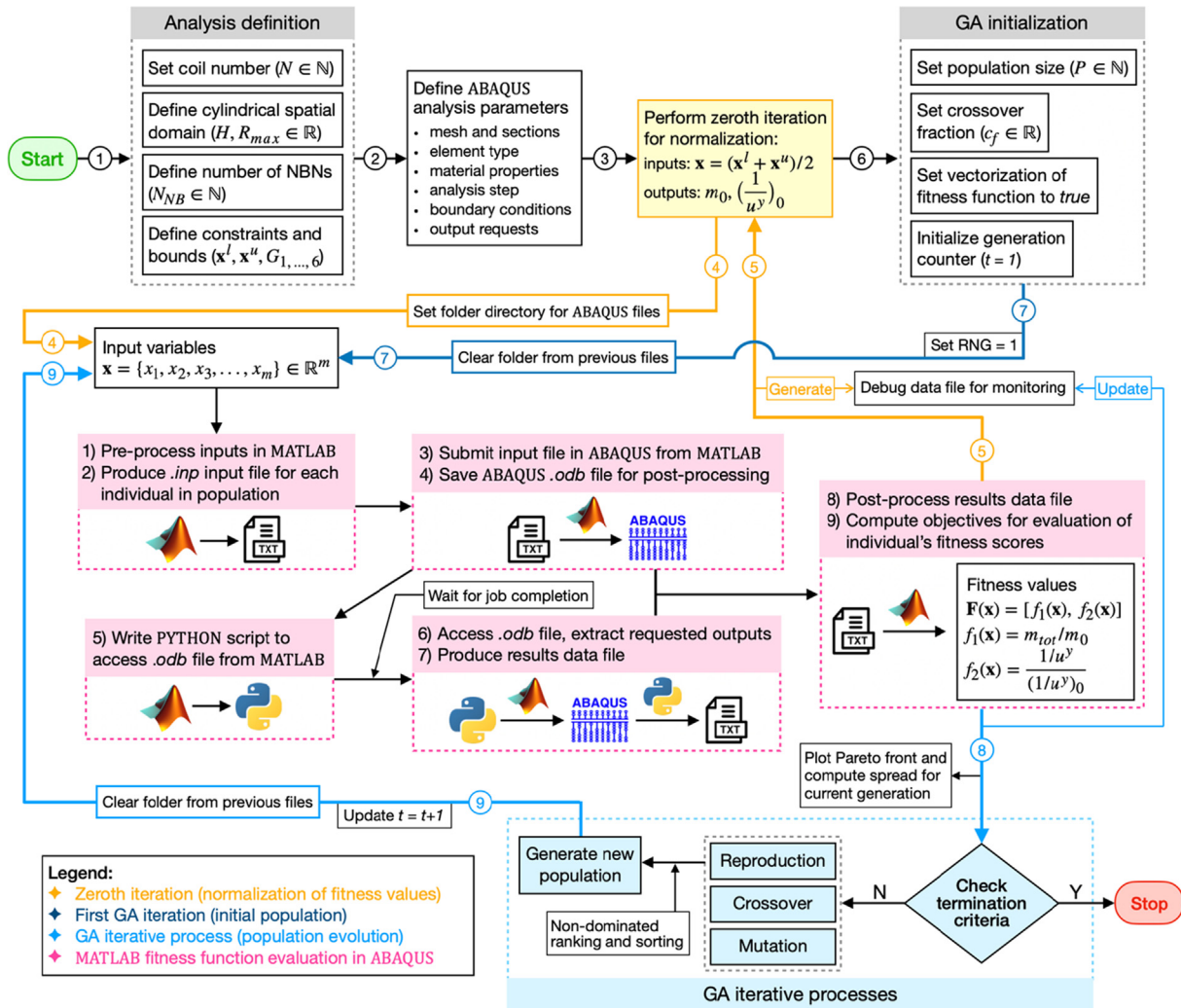


**Fig. 2.** Flowchart of the MATLAB-ABAQUS FE scripts with colour coding representing different optimization phases.

**Table 3**  
Nylon PA-2200 elastic material properties and plastic stress-strain data [29].

Material properties	
Density $\rho$	930 kg/m <sup>3</sup>
Elastic material properties	
Elastic Modulus $E$	1130 MPa
Yield Stress $\sigma^y$	14.0 MPa
Ultimate Stress $\sigma^u$	51.6 MPa
Poisson's Ratio $\nu$	0.3
Plastic material properties	
Plastic Stress [MPa]	Plastic Strain [mm/mm]
14.0,34.1,42.7, 46.7, 49.0, 50.5, 51.3, 51.6	0.0,0.025,0.05,0.075,0.1,0.125,0.15,0.175

sents curvilinear element length. Max stress values are obtained by reading successive individual frames of the simulation file and building a set of lists of stress values for each element and for each frame. Each list is then sorted for the max stress value associated with that frame and corresponding displacement value, obtaining the second objective as  $f_2(\vec{x}) = (1/u)_{s=14\text{MPa}}$ , which represents the inverse of the displacement of the load point at the yielding value, thus indicating the reversible elastic range to be maximized by the optimization procedure.

As to reduce differences in the order of magnitude between conflicting objectives, thus improving performances and stability of the optimization scheme, the GA variables and objective function values have been normalized using Eq. (3) and (4) [30]:

$$x_i^n = \frac{x_i - \left(\frac{x_i^u + x_i^l}{2}\right)}{\frac{x_i^u - x_i^l}{2}}; i = 1, \dots, 2N_{NB}; x_i, x_i^u, x_i^l \in \mathbb{R} \quad (3)$$

where the generic  $x_i$  belongs to GA chromosome vector of design variables  $\vec{x}$ ,  $x_i^n$  represents the normalized value of  $x_i$ , and  $x_i^u$  and  $x_i^l$  represents lower and upper bounds for each variable  $x_i$ ,

$$f_j^n(\vec{x}) = f_j(\vec{x})/f_j(\vec{x}_{avg}), j = 1, 2 \quad (4)$$

where  $\vec{x}_{avg} = \left(\frac{x_i^u + x_i^l}{2}\right)$  is the average vector of the lower and upper

bounds defined in Table 2 for each considered case, and  $f_j^n(\vec{x})$  represents normalized value of  $f_j(\vec{x})$ .

Computations have been performed on a system equipped with an 8-core Intel i7-9700 3.00 GHz processor with 32 GB RAM, with runtimes between 9 h and 13 h for each run, depending on the numbers of coils analyzed and NBNs used. All simulations converged in  $\sim 100$  generations with termination criteria related to the spread of solutions being less than the default tolerance value.

### 3. Shape optimization results

Five sets of Pareto Fronts were obtained for one to five coils as illustrated in Fig. 3. Selecting the best compromise point from each Pareto Front, coordinates of an ideal reference point  $P_{ref}$  are identified by choosing the minimum value of each objective from the solution set,  $P_{ref} = (m_{min}, 1/w^y_{min})$ . The point in the Pareto Front with the minimum euclidean distance from the reference point in the normalized solution space is selected from the set of normalized non-dominated results. Fig. 3 shows the reference point position indicated with a black dot, best mass with green dot, best tensile range with red dot and best compromise solution with yellow dot, respectively. Each point  $F(\vec{x})$  in the non-normalized Pareto Fronts collected represents a non-dominated solution of the multi-objective optimization problem outlined in Section 2.2 and is associated with a unique helical structure geometry.

As it can be noticed from the coordinates of the reference points associated with the various sets, Pareto Fronts are globally moving towards solutions with higher mass and higher tensile range capability for increasing number of coils (i.e. solutions with higher  $m$  and lower  $1/w^y$ ). Best mass solutions tend to be regular in shape with a nearly constant pitch, and radius values approaching the lower bounds in Table 2. Best tensile range and best compromise solutions tend to a teardrop shape with a higher value of radius near the center of the helical structure to minimize shear stress magnitude, and lower radius values near the two ends for maintaining the mass low.

As to highlight superior performances of optimized geometries with respect to conventional coil springs a comparison has been made. Conventional geometries with uniform pitch and radius were selected having equal mass to the best compromise solution for each case considered. Tensile and compressive simulations have been performed for retrieving the correspondent displacements at yielding, with results collected in Table 4. An increment in both displacement values is noticed for increasing number of coils, with optimized geometries consistently outperforming their

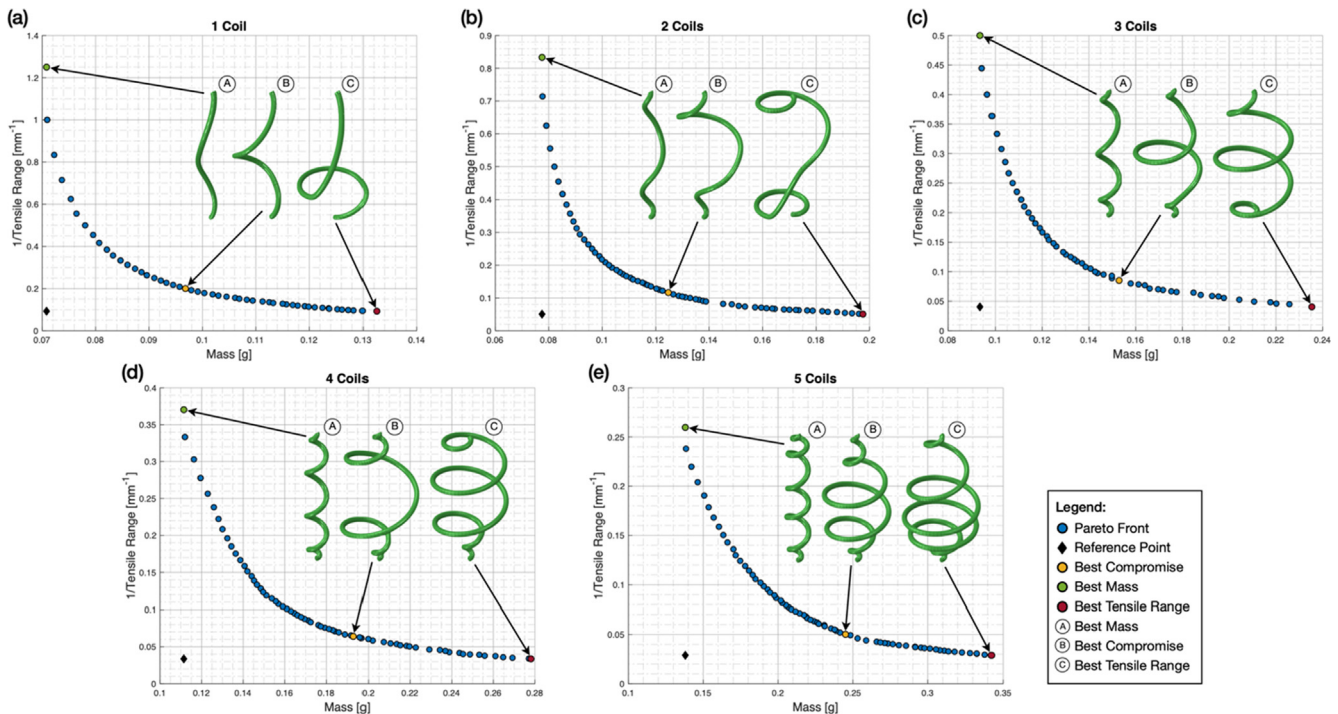












Fig. 3. Pareto Fronts (blue) for different number of coils. (a) One coil, (b) two coils, (c) three coils, (d) four coils, (e) five coils. Reference points (black), dominant objectives (green and red) and best compromise solutions (yellow) highlighted, and corresponding geometries.

**Table 4**  
Comparison between optimized geometries and equal-mass conventional spring structures for different number of coils.

	1 Coil	2 Coils	3 Coils	4 Coils	5 Coils
Best compromise geometry					
Mass value [g]	0.097 g	0.125 g	0.153 g	0.193 g	0.245 g
Tensile range value [mm]	5.00 mm	8.72 mm	11.76 mm	15.60 mm	20.16 mm
Compressive range value [mm]	5.80 mm	10.71 mm	14.36 mm	18.08 mm	17.04 mm
Buckling load [N]	3.5419 N	2.4423 N	1.8673 N	1.4434 N	1.1827 N
First modal frequency [Hz]	0.36774 Hz	0.23724 Hz	0.19068 Hz	0.15165 Hz	0.15916 Hz
Equal-mass conventional geometry					
Mass value [g]	0.097 g	0.125 g	0.153 g	0.193 g	0.245 g
Tensile range value [mm]	4.32 mm	6.50 mm	7.91 mm	10.67 mm	14.95 mm
Compressive range value [mm]	4.84 mm	7.32 mm	8.75 mm	11.31 mm	15.78 mm
Buckling load [N]	3.6329 N	2.4524 N	2.1010 N	1.6872 N	1.3113 N
First modal frequency [Hz]	0.39814 Hz	0.30884 Hz	0.30652 Hz	0.25041 Hz	0.19604 Hz
Improvement % in tensile range	13.6%	25.5%	32.7%	31.6%	25.8%
Improvement % in compressive range	16.6%	31.7%	39.1%	37.4%	29.6%

conventional counterparts. It should be mentioned how, for the five coils case, contact between coils was reached during compression, for the optimized geometry, at a stress level lower than yielding value. This justifies the lower compressive range of five coils optimized structure compared to the four coils one. Performance improvements are expressed computing the percentage increment of displacement obtained by optimized geometries with respect to equal-mass conventional ones:

$$\text{Improvement } \% = \frac{U^{\text{optimized}} - U^{\text{conventional}}}{U^{\text{optimized}}}$$

Moreover, linear perturbation analyses were conducted on individual helical structures for one to five coils optimized and conventional geometries, with results collected in Table 4. Visualization of buckling and modal shapes are collected in Fig. A1 and Fig. A2 of Appendix A. From buckling analysis, it is noteworthy how lower buckling loads were obtained for optimized structures compared to their conventional counterparts, with maximum difference being 14.45% for the four coils cases. A general transition from torsion-dominated to bending-dominated modes is reported for increasing coil numbers, associated with a progressive diminishing of critical loads, with 66.60% and 63.90% overall differences between one and five coils for optimized and conventional geometries respectively. Modal analyses consistently evidenced lower eigenvalues and lower first natural frequencies for optimized geometries compared to their conventional counterparts, with maximum frequency difference of 39.44% for the four coils case. Additionally, progressive diminishing of eigenvalues and frequencies between one and five coils were reported, with 56.72% and 50.76% differences in frequency for optimized and conventional geometries respectively. Compared to conventional geometries, optimized structures show more complex modes due to coupling effects because of the non-uniform mass distribution, while conventional geometries tend to exhibit simpler mode shapes mainly associated with lateral bending. It is evidenced here that it is nonetheless possible to adapt the optimization algorithm itself to optimize other different objectives, for example maximize the critical buckling load, or the first natural frequency to improve the dynamic performances of the helical structures for specific applications. It is stated here that this will obviously produce potentially

different designs, for example with a better ability to control densification in compression thus harnessing the instability phenomena if the critical buckling load is to be maximized. As the ultimate scope of the paper is to design large strain mechanical metamaterials, maximization of critical buckling load or other objectives have not been considered.

Considering the geometrical constraints of both the cylindrical domain size and wire thickness it is estimated that twenty-six is the maximum number of coils that can be defined without the occurrence of interpenetration. As for computational limitations and considering the descending trend of improvements between three and five coils, three coils optimized helical structure is selected as the best-obtained result with 32.7% and 39.1% improvements in tensile and compressive elastic ranges. It will be therefore considered for successive simulations and discussions, as well as for experimental validations.

## 4. Discussion of results

### 4.1. Tensile and compressive deformation mechanism

As previously highlighted, an explanation of the improved mechanical performances achieved by optimized geometries is obtained considering the elastic deformation mechanism involved, shown in Fig. 4. In Fig. 4(a) tensile simulations at yielding point for shape optimized three coils and equivalent conventional geometry are displayed. In the optimized structure shear stresses are mainly acting on the large central turn, resulting in a higher compliance compared to the equal-mass conventional geometry, whereas shear stresses in the conventional geometry influence a larger portion of the structure. In other words, the smaller radius of coils results in more regions of yielded stress. Compressive simulations conducted on the same geometries demonstrated the presence of a similar deformation mechanism as shown in Fig. 4(b). High compliance of optimized structure is due to deformability of its central coil and less regions with yielded stress, which accounts for the improved elastic performances in compression. As similar results held for the four other coils cases, it can be concluded that the per-



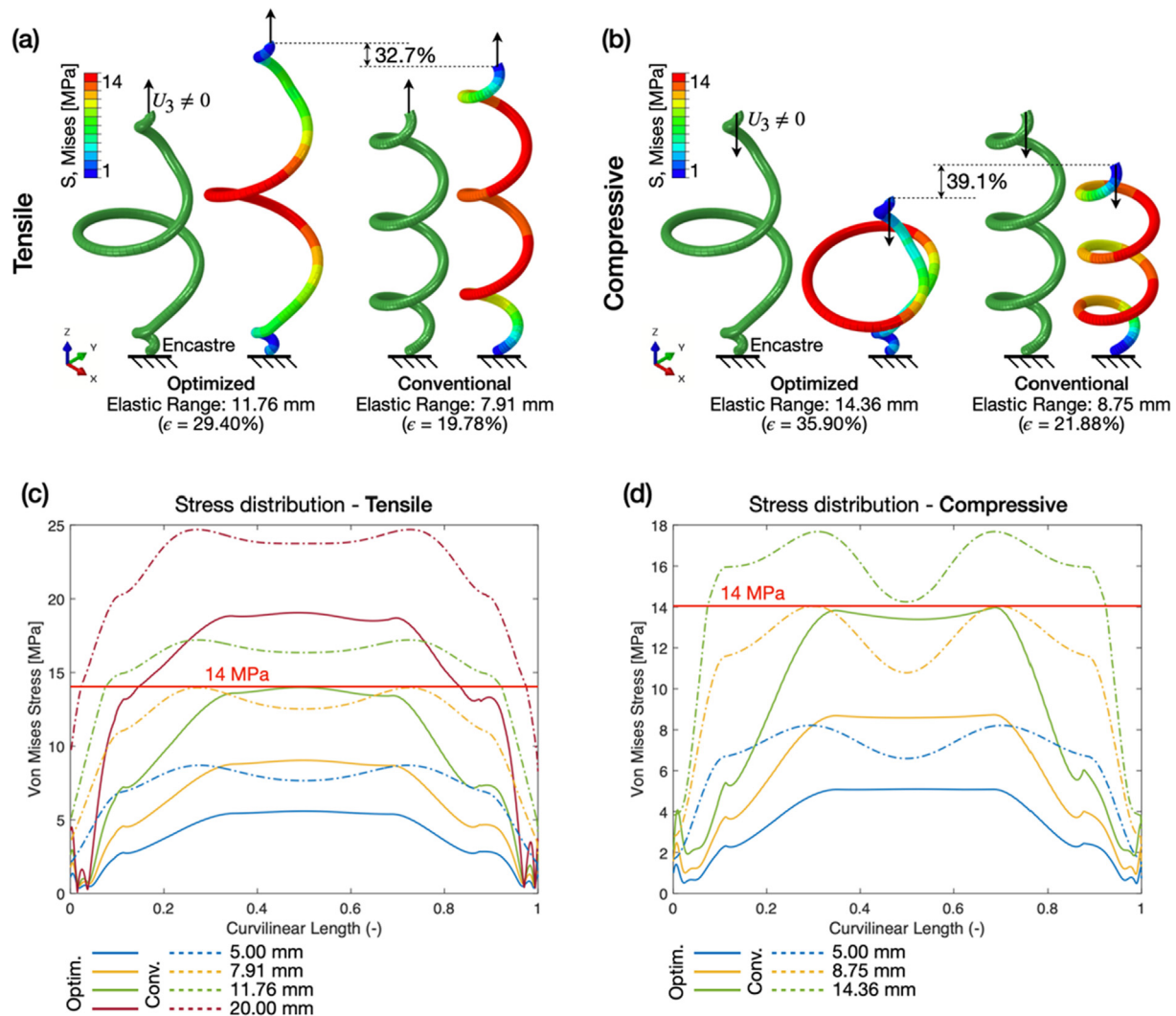


**Fig. 4.** Deformation mechanism and stress distribution for three coils shape optimized and conventional structures. (a, b) Tensile and compressive simulations at yielding on three coils geometries. (c, d) Von Mises stress distribution along curvilinear element length for different tensile and compressive displacements.

formed optimization has exalted overall compliance by acting mainly on the radius profiles of the structures.

Fig. 4(c) presents the stress distributions along the curvilinear element length, for both optimized and conventional three coils geometries with varying tensile displacements applied. It can be noticed the presence of lower stresses acting on the optimized geometry structure (solid lines) compared to the conventional one (dashed lines). The optimized geometry presents lower stressed ends even at higher displacements; however, the conventional geometry has an oscillating trend of high stress for regions near the structure center. Similar considerations held for the compressive cases, Fig. 4(d), where higher oscillation amplitude is noticed for the conventional geometry. From analysis of Fig. 4(c, d), maximum stresses of 9.03 MPa and 8.73 MPa are acting on optimized geometry in tension and compression, while the conventional structure reaches yielding stress of 14 MPa in both cases. These are 35.5% and 37.6% lower than yielding stress, confirming superior structural performances considerations, for example the possibility of an improved fatigue life of optimized geometries when subjected to cyclic low-stress loading conditions.

Further discussions of the geometric differences between optimized and conventional springs are presented in Appendix B. Moreover, large tensile deformations conducted beyond yielding

strain highlighted the presence of two plastic deformation mechanisms, better described in Appendix C for the three coils cases.

#### 4.2. Stiffness computation

In Fig. 5 plots of reaction force vs elastic displacement are shown for tensile and compressive cases. One to five coils optimized (solid lines) and conventional (dashed lines) geometries are collected. A general trend of diminished stiffness and improved compliance between conventional and optimized structures can be noticed. This results in lower reaction forces and higher deformability of the optimized geometries.

Since the characteristic curves of the springs are not linear, the values of stiffness defined as ratios between reaction force and displacement are locally changing. However, for comparison purposes, and considering the low curvatures involved, calculations have been performed by taking the ratio between the reaction force [N] and the displacement [mm] at yielding, i.e.  $K_{\text{mean}} = \left( \frac{\text{Reaction Force}}{\text{Displacement}} \right)_Y \left[ \frac{\text{N}}{\text{mm}} \right]$ . Results from such calculation are collected and shown in Fig. 5 where mean stiffness values are reported for considered cases, confirming previous observations. In particular, differences in stiffness of 60.9% and 66.7% are reported for the three coils cases between optimized and conventional geometries, for tension and compression respec-



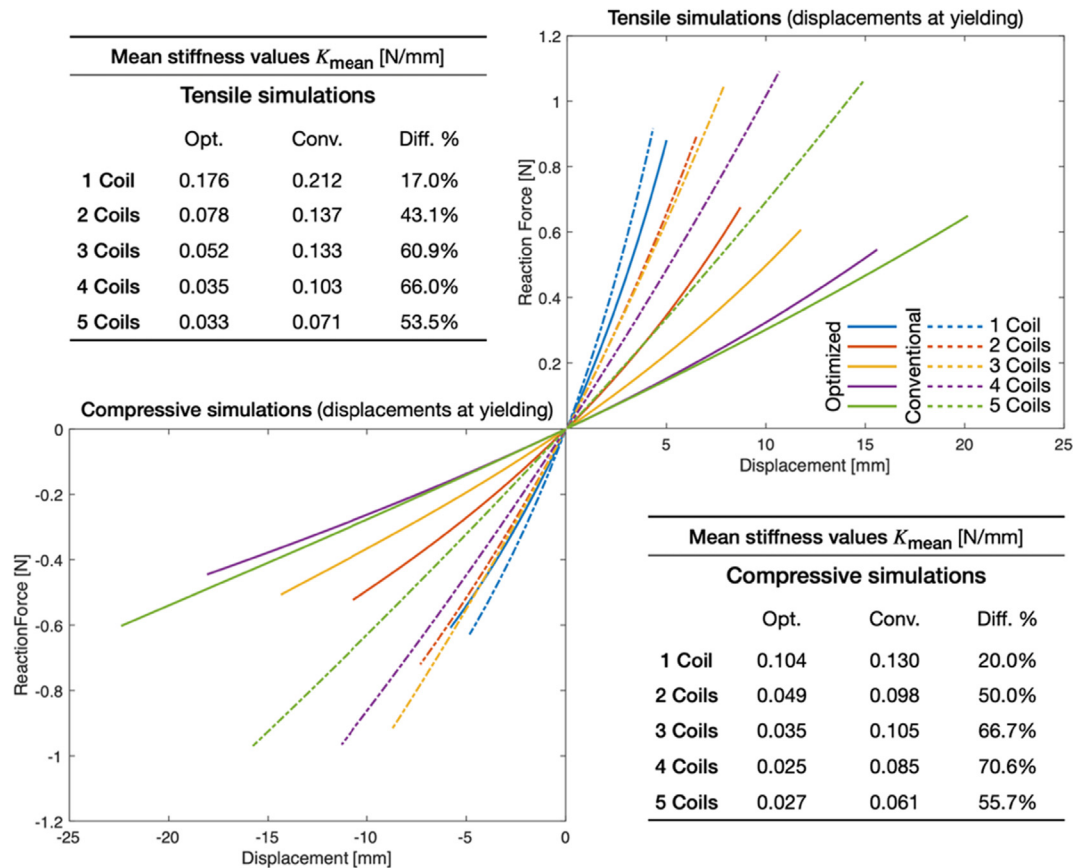


Fig. 5. Tensile and compressive elastic curves for optimized and conventional geometries.

tively. Since modal frequencies are proportional to  $\sqrt{k/m}$ , with  $k$  and  $m$  being the stiffness and mass of the structure, as lower stiffness values were consistently observed for the optimized geometries compared to their conventional counterparts, it descends how lower natural frequencies were already expected for the optimized geometries, as confirmed from results in Table 4 and Appendix A. Also, due to the increase in mass and decrease in stiffness for increasing number of coils, the general trend of diminishing frequency on both optimized and conventional geometries was also expected.

#### 4.3. Influence of material properties on optimization results

To understand the influence of different material behaviors on the optimization procedure, further optimization runs have been performed on the three coils structure. In particular, Polylactic Acid PLA (modelled with linear elastic–plastic behavior, as it was already the case for Nylon PA-2200 from Section 2), Aluminum 70–75 T6 (modelled with Johnson–Cook behavior) and Ethylene–Propylene Diene Monomer EPDM (modelled with hyperelastic Ogden behavior with  $n = 3$ ) were selected as base materials, and subsequent optimization results compared with those obtained using Nylon PA-2200. Elastic and plastic stress–strain data for PLA, as well as Johnson–Cook plasticity constants for Aluminum 70–75 T6 and material law parameters for EPDM are reported in Appendix D. Best compromise geometries were selected with the approach in Section 3 and collected in Fig. 6. In particular, for the optimization with EPDM the maximum stress correspondent to 100% strain of a conventional helical structure with linear quota function and constant radius functions median between the lower and upper bounds (equal to 0.137 MPa) has been selected for the computation of the second objective.

From the analysis of the optimization results, it can easily be noticed how similar geometries were obtained for all considered cases, Fig. 6(a), with a deformable central coil that bear shear stresses acting on the structure during its elastic deformation. Figure E in Appendix E confirms this trend, as GA tends to position NBNs near the same locations, with maximum radius values near the upper bounds for all cases: 9.84 mm for PA-2200, 9.92 mm for PLA, 9.44 mm for EPDM and 9.87 mm for Aluminum. In Fig. 6(b) plots of reaction force vs displacement are displayed for the four geometries obtained. In particular, the reaction force for each case has been normalized to the Young's Modulus of the base material used (with values reported on the table inside Fig. 6(b)), confirming the similarities between different geometries. Moreover, the similar mechanical behavior of PA-2200 and PLA is evidenced, as well as the different behavior of Aluminum and EPDM. Although optimized structures present similar geometric characteristics for varying material properties, the displacement values at yielding obtained are generally different. In particular, higher values are associated with softer polymer materials. Moreover, considering the confirmed presence of under stressed ends, it should be mentioned how optimized choice of material properties is possible. This can be better performed by selecting different material properties for different regions of the structure body, thus potentially improving the obtainment of the selected conflicting objectives, further optimizing the design, but it is outside the scopes of the present paper.

#### 5. Tessellation study of optimized helical structures for metamaterial applications

In this section, 1D metamaterial implementations with different tessellation numbers and arrangements are simulated to highlight

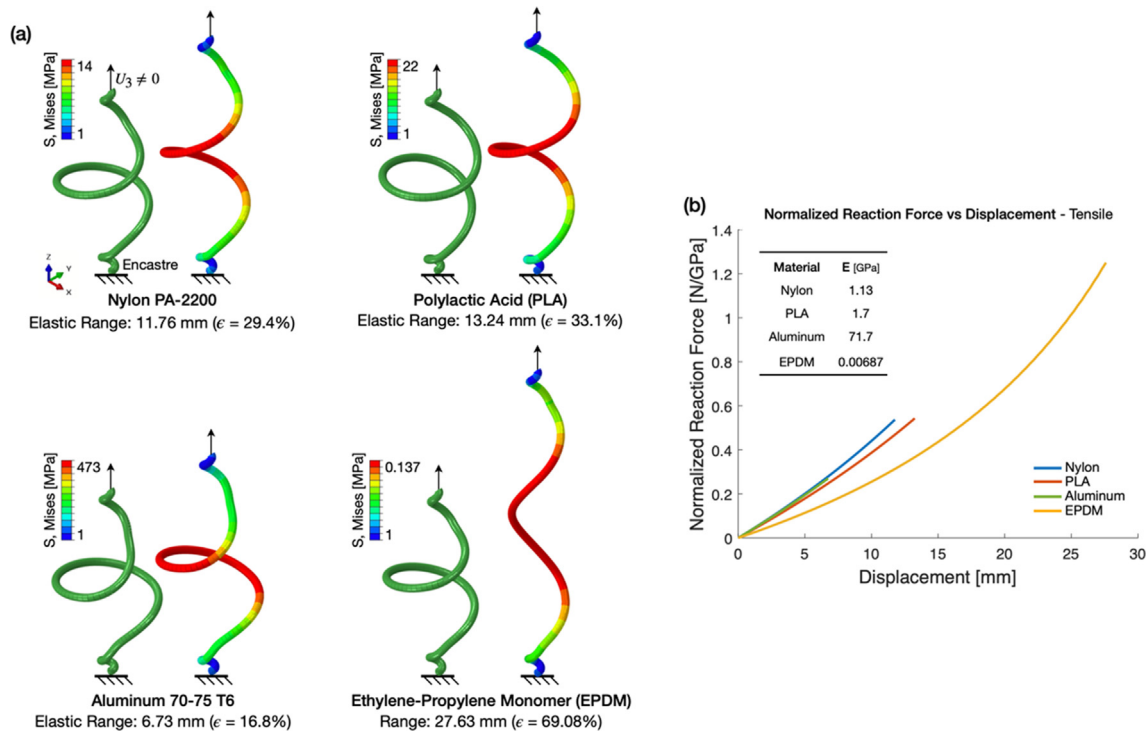


**Fig. 6.** Influence of material properties on shape optimization results. (a) Tensile deformations at yielding for optimized geometries with different materials, (b) corresponding tensile elastic curves and mean stiffness values.

superior performances in terms of static tensile and compressive stiffness as well as buckling and modal performances. Due to the large number of simulations performed only results for three coils tessellations will be presented, with the consideration that similar results held for other cases. In successive studies which are outside the scopes of the present paper complex 2D and 3D metamaterial implementations will be investigated, where different unit cell shapes will be designed. Planar and solid lattice structures demonstrating exceptionally large strain and energy absorption capacity, ZPR behavior and anisotropic properties, will be developed and numerically and experimentally investigated from the static, dynamic and impact point of view. In particular, to better understand the influence of shape optimization on unit cell design, advanced optimization techniques can be used for lowering the computational cost of optimizing whole unit cells instead of single members only, as it was the case for the results presented in this work. In fact, the computational cost of optimizing unit cells instead of single members depends largely on the number of beam elements inside these unit cells, and as such it mainly scales with the number of nodes in the geometry which needs to be solved. Nonetheless, if the optimization is to be conducted contemporary on different helical structures inside the same unit cell, the number of variables in the GA chromosome can easily become extremely high due to the further expansion of the design space, which will greatly negatively affect the overall optimization efficiency in terms of necessary population size and number of needed generations.

### 5.1. Tessellation arrangement study for metamaterial implementation

Since end conditions of individual helical structures have been defined through constraints  $G_5$  and  $G_6$  presented in Table 1, Section 2.2, tangency at both ends of each structure is preserved. Serial connection is therefore possible and linear tessellations can be defined, with various unit cells represented in Fig. 7. In Fig. 7(a-

d) four different unit cells, namely  $\langle AB \rangle$ ,  $\langle AD \rangle$ ,  $\langle CB \rangle$ ,  $\langle CD \rangle$ , are defined which combine linear couples of  $A$ ,  $B$ ,  $C$ ,  $D$  components with  $A$  being the optimized three coils structure,  $B$ ,  $C$  and  $D$  its  $180^\circ$  rotations around  $z$ -,  $x$ - and  $y$ -axes respectively. They represent possible linear connections obtained by use of individual rotations, preserving tangency between successive ends. Another type of arrangement can be obtained using point-symmetry, Fig. 7(e, f), which restitutes  $\langle AA' \rangle$  and  $\langle A'A \rangle$  unit cells,  $A'$  being the point-symmetric of  $A$  with respect to the connection point. It is noteworthy how while chirality is preserved for the rotation-based unit cells, the same is not verified for the symmetry-based ones which present a change of coil orientation in the middle. A third possible arrangement makes use of connector beam elements of variable length  $n$ . In this case, the unit cell is defined by a single helical structure plus two half connectors aligned with the longitudinal axis. Static analyses on all tessellation arrangements demonstrated how effects of tessellation geometry are negligible. As for ease of manufacturing, in the present paper only  $\langle AA' \rangle$  unit cell arrangement is considered.

### 5.2. Homogenization study of effective Young's Modulus

As tessellation size has significant influence on the structural behaviour of metamaterials, homogenization study needs to be performed to retrieve tessellation numbers demonstrating independency from these effects. In particular, the variation of effective Young's Moduli were considered with results presented in Fig. 8. Effective Young's Modulus of optimized helical structure in the longitudinal loading direction,  $E_{zz}$ , can be defined as  $E_{zz} = \frac{\sigma_z}{\epsilon_z} = \frac{F_z L}{\pi R^2 \delta_z}$ , where  $F_z$ ,  $\delta_z$ ,  $L$  and  $R$  refer to reaction force, imposed displacement, length and maximum coil radius respectively. To compute effective Young's Moduli, six tessellation numbers were considered from one to eleven unit cells in  $\langle AA' \rangle$  configuration and tested for tensile and compressive loading. For the ABAQUS implementation of tessellation arrangements tie constraints have

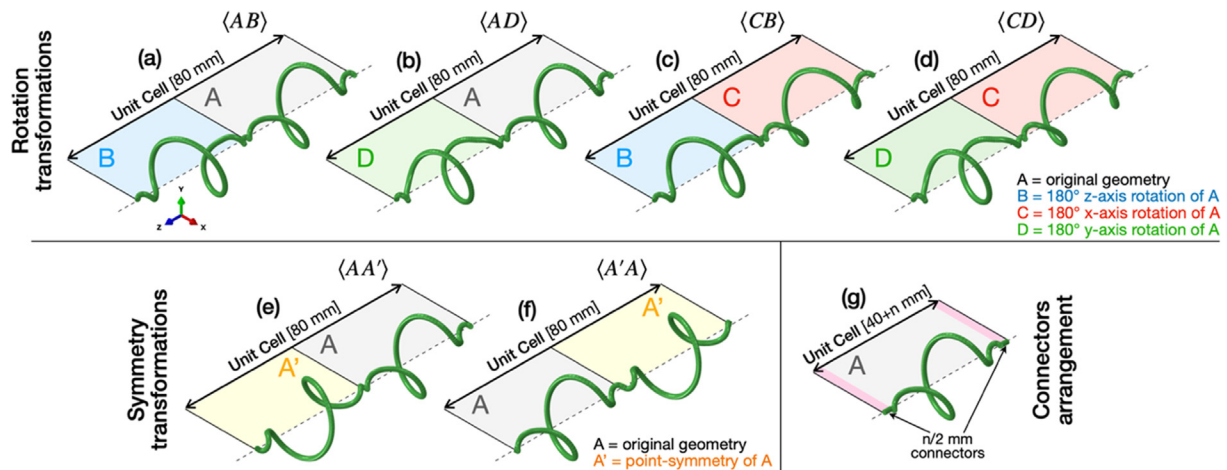


Fig. 7. Seven potential unit cell arrangements obtained with couples of three coils optimized helical structures.

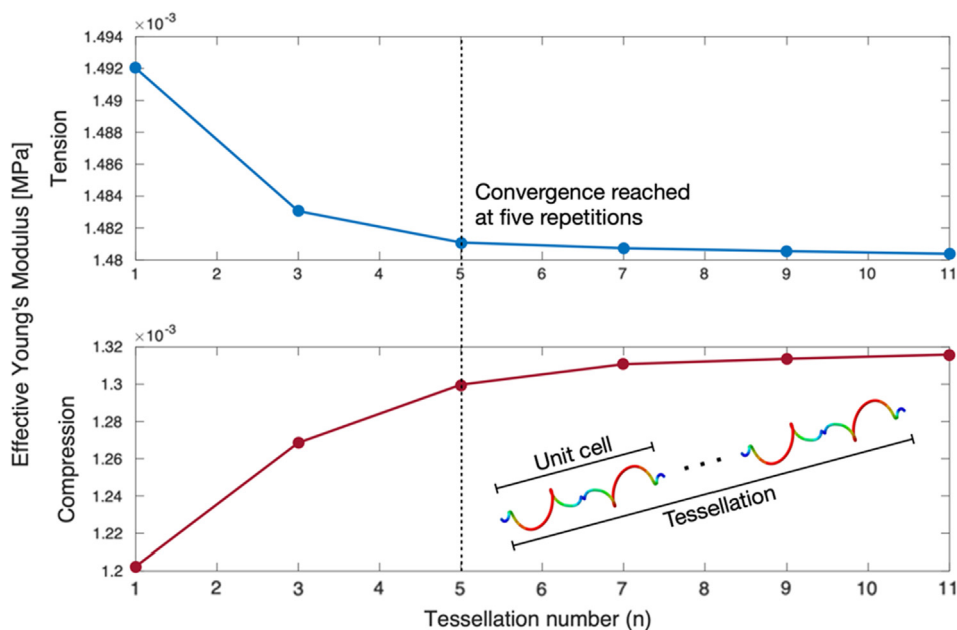


Fig. 8. Convergence of effective  $E_{zz}$  of the helical structure with increasing number of unit cell repetitions for three coils optimized geometry in (AA') configuration.

been defined, to link successive instances together fixing adjacent nodes. Quadratic beam elements B32 were defined for all models, consistent with Section 2.3, selecting mesh densities correspondent to 128 nodes per coil and using Nylon PA-2200 material, with properties in Table 3 of Section 2.3. For both types of simulations the first node of each tessellation ( $z = 0$  mm) has been encastred, while the last has been given an imposed displacement in the longitudinal direction.

Results for homogenization study are illustrated in Fig. 8, which shows that Young's Moduli of optimized helical structures, both in tension and compression, are significantly smaller than original constructing material (1130 MPa for Nylon PA-2200). Furthermore, the effective  $E_{zz}$  of the structure changes with more cell repetitions being applied until a critical point at five repetitions is reached. It is noticeable how the tensile Young's Modulus diminishes with increasing tessellation size, while the compressive one increases. Moreover, compressive stiffness values are always lower than the respective tensile ones. In the tensile simulations all considered

tessellations reached yielding at strains approximately constant and near the value of yielding strain of the original constituent helical structure (29.4% strain). In the compressive cases instead, the effects of buckling were predominant with a consistent diminishing of compressive range for increasing tessellation size.

### 5.3. Linear perturbation analyses

Buckling analysis of optimized structures is beneficial for their engineering applications as it permits to quantify their static performances. In this section, buckling characteristics of such structures are studied considering effect of tessellation size, which ranges from one to eleven unit cells. To minimize the complexity of the analysis, beam elements were used in accordance with Section 2 and Section 5.2. Regarding boundary conditions, the first node of each tessellation ( $z = 0$  mm) has been given fixity conditions, while the last node ( $z = n \times 80$  mm, with  $n$  equal to the number of unit cells involved) has been given a concentrated 1 N

unit load in the negative  $z$ -direction. Table 5 presents buckling loads and mode shape representations, from lateral view, of the analyzed geometries. The trend of buckling loads shows a nonlinear decrease as tessellation numbers increase. In particular, buckling load of  $5.28\text{E-}3$  N for eleven unit cell tessellation is almost 61 times smaller than the  $0.322$  N of single unit cell arrangement. Moreover, buckling loads have been also normalized to the corresponding tessellation structural weight for better representation, confirming the nonlinear decreasing trend. Mode shapes are all characterized by pure bending behaviour, along the principal axis of inertia.

Free vibration study permits retrieving fundamental dynamic characteristics of optimized structures as function of tessellation size. Tessellation sizes selected are set to be the same as from previous buckling studies. Fixed-fixed boundary conditions have been considered for all models, with both the first node of each tessellation ( $z = 0$  mm) and the last one ( $z = n \times 80$  mm, with  $n$  equal to the number of unit cells involved) encastred. Table 5 presents first natural frequency and mode shapes representations, from lateral view, of the analyzed geometries. The trend of natural frequencies shows a nonlinear decrease as tessellation numbers increase. In particular, natural frequency of  $7.57\text{E-}4$  Hz for eleven unit cell tessellation is almost 119 times smaller than the  $9.04\text{E-}2$  Hz of single unit cell arrangement. Mode shapes are all characterized by pure bending behaviour, along the principal axis of inertia, although pointing in opposite direction for three and five unit cell tessellations only.

Results and trends similar to those presented in Table 5 were retrieved for other coil geometries, not shown here for conciseness of reporting. It descends then how optimized geometries perform better than conventional ones from the static point of view, showing higher tensile and compressive ranges both in single form, unit cell and tessellation arrangements. This improves the elastic deformability of the overall structure and its stability when employed for meta-material applications. It should be mentioned, nonetheless, how greater deformability comes at the expense of diminished stiffness and critical load and how the natural frequencies were thoroughly affected. Such considerations are important when implementing optimized structures in dynamic environments.

## 6. Experimental validation

### 6.1. Manufacturing

Quantifying errors between simulation models and physical structures, in this section three coils geometries were selected

for 3D printing and testing. They were modelled by 3D solid structures using CATIA where a single unit cell was built with a serial connection of two helical structures in (AA') configuration, as shown in Fig. 7(e). Clamping blocks were added at both ends for fixing the sample to the test machine reproducing encastred boundary conditions as considered in the optimization procedure. To eliminate boundary effects, two short connector elements were added on both ends of the structure avoiding unrealistic stress concentrations at clamping blocks attachments. CAD models revealed the complex curvatures with narrow angles involved in the central region of the samples. Moreover, considering limitations on printing and testing area all sizes of the samples with respect to the numerical models presented in Section 3 were doubled. The manufactured helical structure had a length of 80 mm with 3 mm wire thickness diameter. Considering the clamping blocks and connectors lengths of 25 mm and 5 mm on both ends, the total length of manufactured samples was 220 mm, allowing 3D printing in a single process. Experimental samples, shown in Fig. 10(a), were manufactured by Selective Laser Sintering (SLS) using a sPro140 3D printer, printing the fully solid model in 0.1 mm high layers of PA-12 material.

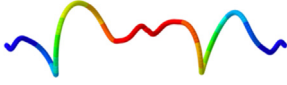
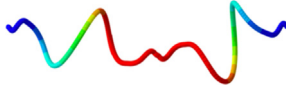






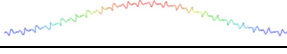
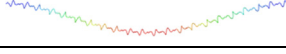
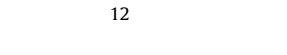

### 6.2. Material characterization of Nylon PA-12

Material characterization of PA-12 was conducted for consistency of results. Five dog-bone tensile test samples were manufactured using a sPro140 3D printer (Protolabs) and then tested in accordance with ASTM D638-14 standard [32]. Tests were performed using an Instron 5965 test machine equipped with a 5kN load cell. The stress-strain curves for the dog-bone samples were obtained, from which average values of elastic properties and plastic stress-strain data were calculated and are reported in Fig. 9(b).

### 6.3. Structural tensile and compressive tests

Four samples were tested for both tensile and compressive loadings, two for three coils optimized geometry and two for three coils conventional springs. The experimental setup shown in Fig. 10(b), includes the test sample installed on the Instron 5965 test machine with a 5kN load cell and the data acquisition system. A Nikon D7000 DSLR camera was used to capture videos during the tests, from which images were extracted at significant frames. The load-displacement curves were recorded for a constant rate of 2 mm/min until failure in the tensile cases, or contact/buckling onset in the compressive cases with 15 Hz data record frequency.

**Table 5**  
Linear perturbation analyses for varying tessellation size.

Linear perturbation analyses on chosen tessellations					
Tessellation size	Buckling analyses		Buckling mode shape	Modal analyses	
	Critical load [N]	Normalized critical load to weight [N/g]		First natural frequency [Hz]	First mode shape
1	0.322	1.054		$9.04\text{E-}02$	
3	$6.97\text{E-}02$	0.076		$1.01\text{E-}02$	
5	$2.54\text{E-}02$	0.017		$3.65\text{E-}03$	
7	$1.30\text{E-}02$	0.006		$1.87\text{E-}03$	
9	$7.89\text{E-}03$	0.003		$1.13\text{E-}03$	
11	$5.28\text{E-}03$	0.002		$7.57\text{E-}04$	



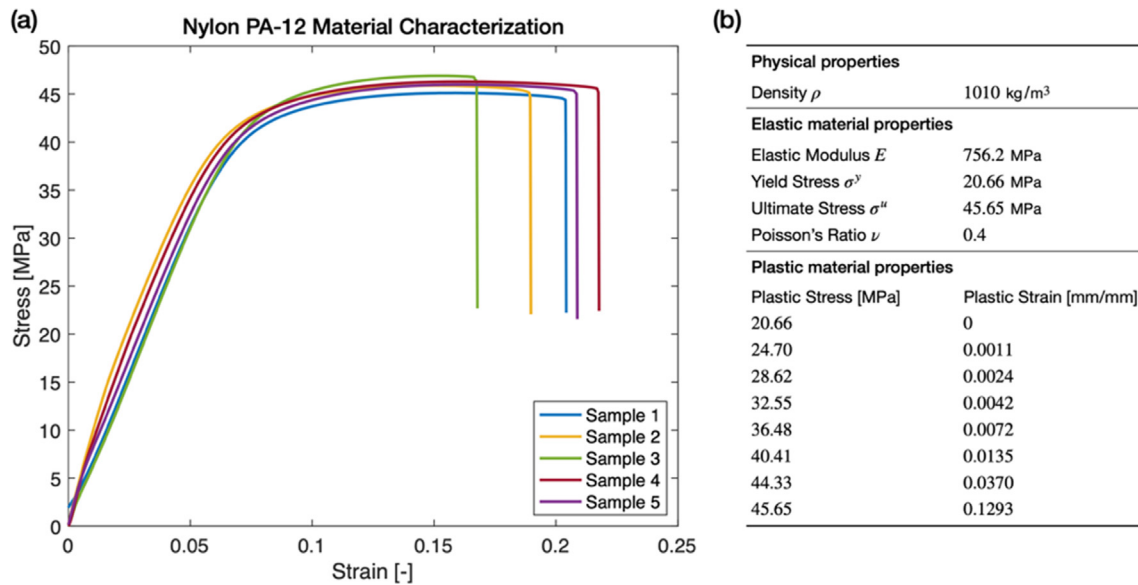


Fig. 9. Material characterization of Nylon PA-12. (a) Stress–strain data from test machine, (b) averaged material properties.

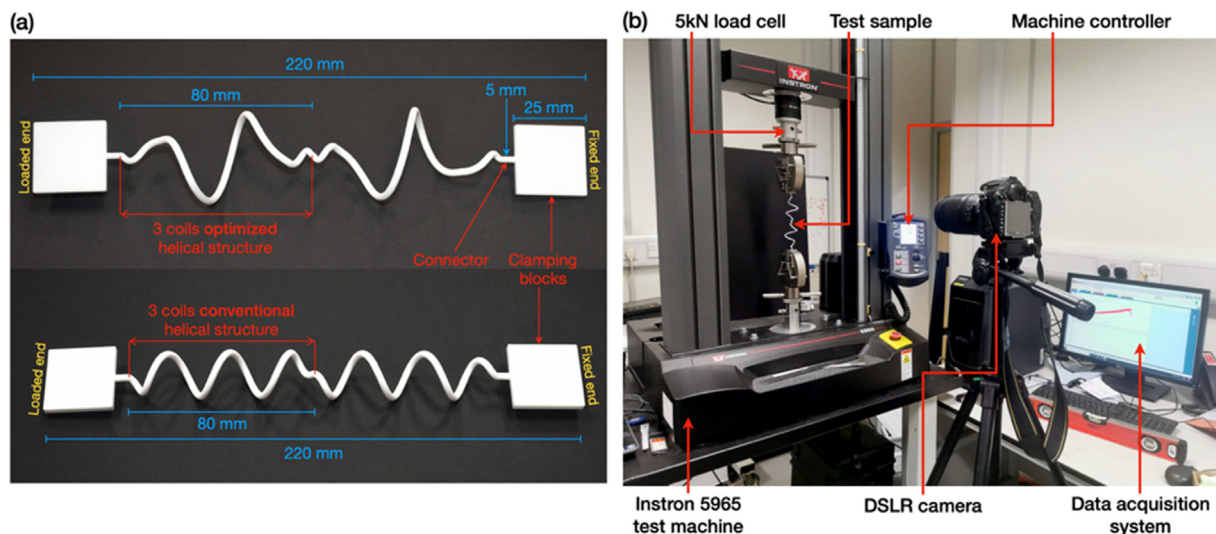


Fig. 10. Manufacturing and experimental testing. (a) 3D printed test samples, with dimensions highlighted; (b) experimental setup, test machine with data acquisition and image recording systems.

#### 6.4. Experimental results and discussion

The recorded load–deflection data for tensile and compressive cases are plotted and compared with numerical results in Fig. 11 (a, b). In the GA-based optimization procedure presented in Section 2, thin beam elements were used for modelling helical structures achieving a large iteration rate necessary in GA for convergence. However, errors might be present in the analysis of the structure due to limitations of the beam-based approach. Stress concentration effects due to narrow curvatures are in fact neglected in beam models and governing equations have small accuracy for lower aspect ratios. For these reasons, the experimental procedure was replicated with 3D solid FE models generated in ABAQUS/Standard, using material properties from Section 6.1, fixed boundary conditions on the lower clamping box end and imposed displacement on the upper one as described in Section 6.2. Solid quadratic 3D elements C3D10 were used with very fine mesh. It can be noticed that a very good correlation was achieved

between numerical and experimental results. A general underestimation of stiffness is present in the numerical results especially in the elastic range.

Fig. 11(a) shows average errors of 9.57% and 2.79% for optimized helical structure and conventional spring in tension, respectively. Fig. 11(b) shows maximum errors of 18.34% and 18.98% for optimized helical structure and conventional spring in compression. The higher errors in compressive loadings are mainly due to analysis limitations of complex curvatures with more sensitive mechanism of deformations. The obtained stiffnesses are nonetheless in the same order of magnitude with a very good correlation, hence the procedure can be considered validated.

Figs. 12 and 13 show a comparison of deformation mechanism in experimental results and numerical simulations. The corresponding frames in tensile and compressive experimental videos were selected based on simulations increments at yielding displacements as well as buckling and contact occurrence, respectively. The comparison shows identical mechanisms of

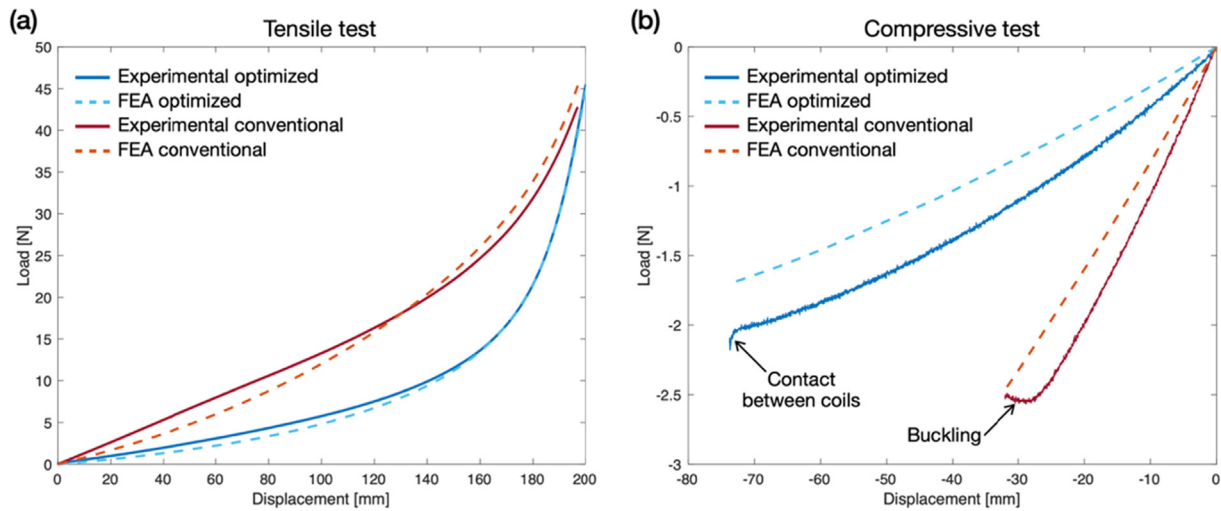


Fig. 11. Results obtained from experimental analyses and comparison with numerical simulations. (a) Tensile test ; (b) compressive test (buckling and coil contact occurrence indicated).

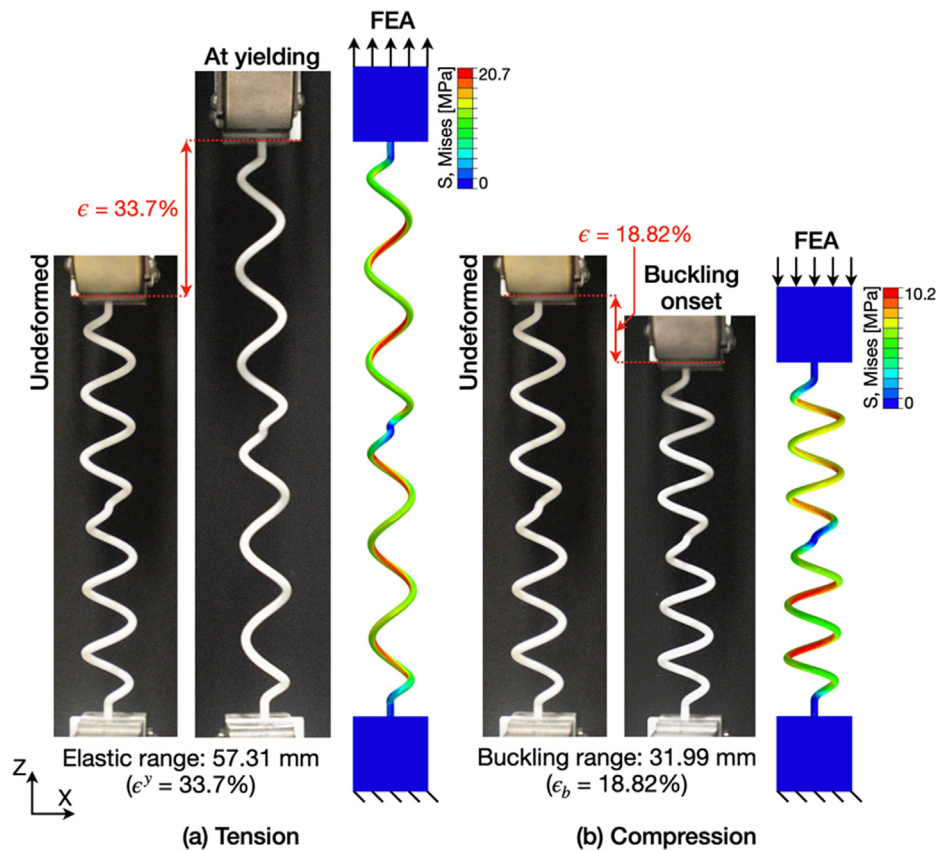


Fig. 12. Comparison between experimental and numerical analyses for conventional three coils geometry. (a) Tensile analysis, (b) compressive analysis.

deformations in both experiments and simulations, highlighting further the validation of numerical results. Comparing the performances of optimized helical structure with conventional spring, analyses show how the optimized structure presents 15.2% more strain at yielding, correspondent to a 31.05% improvement of tensile yielding strain. This is particularly significant as it agrees very well with the GA results presented in Section 3, where 32.70% improvement was recorded for the three coils case. Moreover, while the conventional structure is subjected to elastic buckling

in the form of lateral bending if subjected to compressive loading, the optimized structure presents 24.6% more strain reaching then contact between coils without the occurrence of buckling, which is correspondent to a 56.64% improvement. This confirms the already noticed improvements in compressive range and stability obtained by optimized geometries, Section 5.2. The GA procedure can be considered validated and effective offering significant potential in lightweight performance improvements.

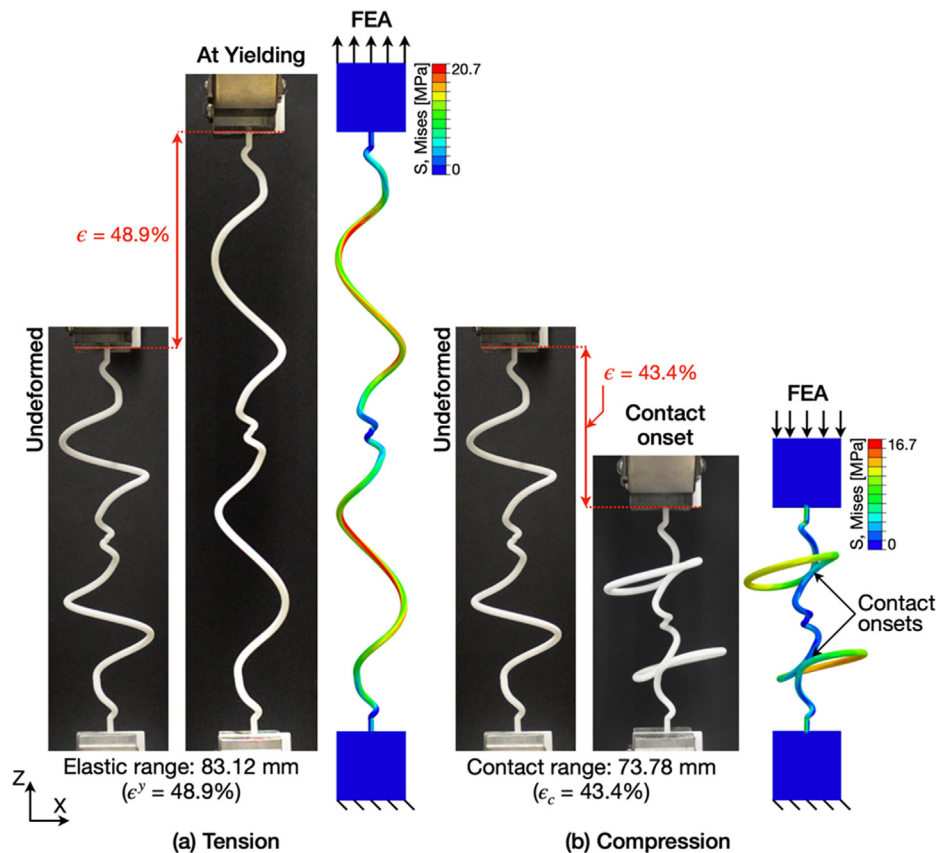


Fig. 13. Comparison between experimental and numerical analyses for shape optimized three coils geometry. (a) Tensile analysis, (b) compressive analysis.

## 7. Conclusion

In this paper, a novel method for designing 3D helical structures was proposed through definition of two functions controlling the geometry evolution of the structure. Three-dimensional helical structures were shape optimized by means of GA multi-objective optimization technique to achieve minimum mass and maximum elastic strain range. An advanced FE code in 3D space combining capabilities of commercial ABAQUS software inside MATLAB GA toolbox was developed.

Best compromise solutions among five sets of Pareto Fronts were selected by taking the point in the Pareto Optimal Set with the minimum Euclidean distance from a reference point. The analysis of best compromise solutions highlighted the superior performances of optimized structures in terms of compliance capabilities. The novel helical structure with three coils demonstrated the best mechanical performance with a maximum of 32.7% and 39.1% higher tensile and compressive ranges respectively, compared to equal-mass conventional coil springs at yielding. Also, the deformation mechanism of three coils structure evidenced 35.5% and 37.6% lower stresses in tension and compression respectively, demonstrating significant potential to improve the fatigue life of helical structures. Testing of different material behaviors demonstrated the independence of optimized shape from original constitutive materials, with Nylon PA-2200, Polylactic Acid PLA (linear elastic–plastic model), Ethylene-Propylene Diene Monomer EPDM (hyperelastic Ogden model), and Aluminum 70–75 T6 (Johnson-Cook model) tested.

1D mechanical metamaterial applications were proposed with seven different unit cell arrangements. Homogenization study was conducted in tensile and compressive simulations to demon-

strate the independence of mechanical behavior from tessellation numbers. Further FE simulations were performed to investigate linear perturbation behaviors of optimized helical structures for varying tessellation size. The results showed diminishing trend for both buckling load and modal frequencies for higher tessellation numbers.

Moreover, tensile and compression experiments were conducted on 3D printed unit cell samples made of Nylon PA-12 material. High fidelity FE analyses with fine-meshed models demonstrated a very good correlation with experimental data. The experimental results also highlighted significant improvements of 31.1% in tensile strain range and 56.6% in compressive strain ranges.

In a successive work, currently under development, complex 2D and 3D lattice metamaterials will be modelled, manufactured and studied. In particular, planar and solid tessellations will be tested for different loading conditions to investigate their anisotropic properties and assess the presence of Zero Poisson's Ratio (ZPR) behavior. Moreover, impact and crashworthiness performances will be addressed in light of aerospace and automotive applications. It is highlighted here how careful attention will be given on manufacturability, optimization techniques and effects of defects.

In fact, to carefully address the lattice metamaterial behavior and potentially improve its mechanical performances, the proposed helical structures design can be incorporated in microscale and then studied with more complex optimization schemes. A range of modern literature addresses the topics at hand, such as the controllability of mechanical properties through the insertion of controlled defects and vacancies in the metamaterials' structure [33,34,35,36]. In such works, architected defects effects are

addressed through complex FE modeling and advanced optimization techniques such as Bayesian Optimization. The use of controlled placed defects - which for the topics at hand can be represented by missing helical structures inside specific unit cells - permits to increase the strain energy capacity of the structure, allowing localized buckling of lattice members to happen on specific unit cells. Apart from Bayesian Optimization, other optimization techniques may be addressed for the design of architected meta-materials, such as deep learning based ones as well as topology optimization.

**Declaration of Competing Interest**

The authors declare that they have no known competing financial interests or personal relationships that could have appeared to influence the work reported in this paper.

**Appendix A**

See Fig. A1, Fig. A2

**Appendix B**

In Fig. B1(a), quota and radius functions are shown for the three coils optimized and conventional cases. It is noticeable how, while the conventional geometry is defined by linear  $z(\theta)$  and constant  $\rho(\theta)$  laws, the optimized one tends to sigmoidal  $z(\theta)$  and gaussian

$\rho(\theta)$  ones, highlighting the presence of the large central turn. Maximum radius of optimized geometry, equal to 9.84 mm, is approaching the 10 mm upper bound, compared to the 4.81 mm radius of equivalent-mass conventional spring. Associated coordinates of NBNs are reported in Fig. B1(b).

**Appendix C**

Large tensile deformations conducted beyond yielding strain highlighted the presence of two plastic deformation mechanisms, as shown in Fig. C1 for both optimized and conventional three coils structures. Mechanism I, indicating displacements between points (1a), (1b) and (2a), (2b), is characterized by coils bending due to shear stresses acting along the wire with high compliance and low reaction forces, and is influent at strains below 100% (yielding strain being 29.4% and 19.8% for three coils optimized and conventional geometries). A transition zone between 100% and 125% strain is noticed. Mechanism II is characterized by tensile stretching of the structure, with low compliance and high reaction forces, points (3a), (3b) and (4a), (4b), until ultimate stress and consequent breakage is reached (slightly above 150% strain for three coils optimized and conventional geometries). Also indicated by the dashed lines in Fig. C1, the yielding strains. The obtained characteristic curves are typical of compliant structures and are usually referred to as *J-shape* curves. They pose great interest in biomedical applications due to their similarity with human tissues mechanical properties.

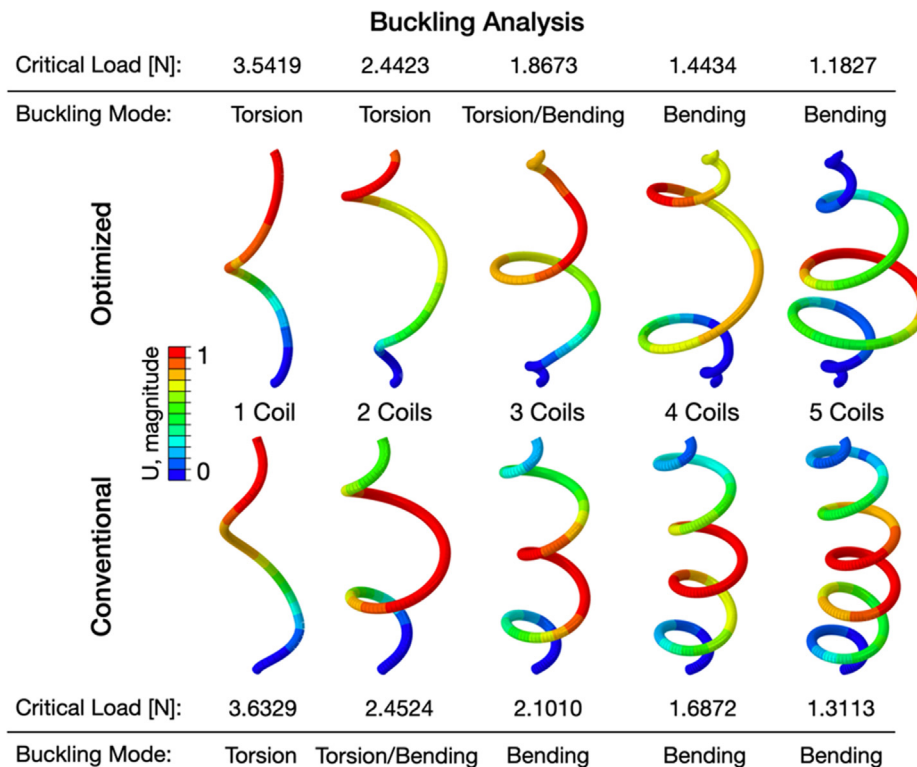


Fig. A1. Buckling analyses on helical structures with first critical buckling loads [N] and buckling mode shapes indication.



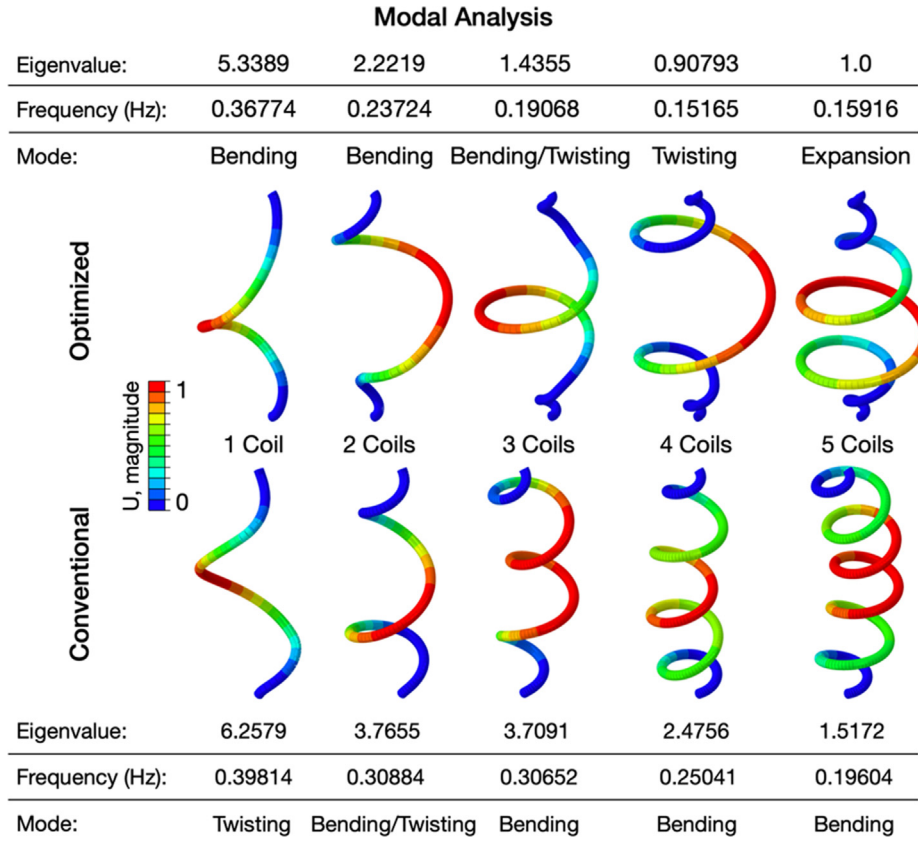


Fig. A2. Modal analyses on helical structures with first eigenvalue, associated resonance frequency [Hz] and mode shapes indication.

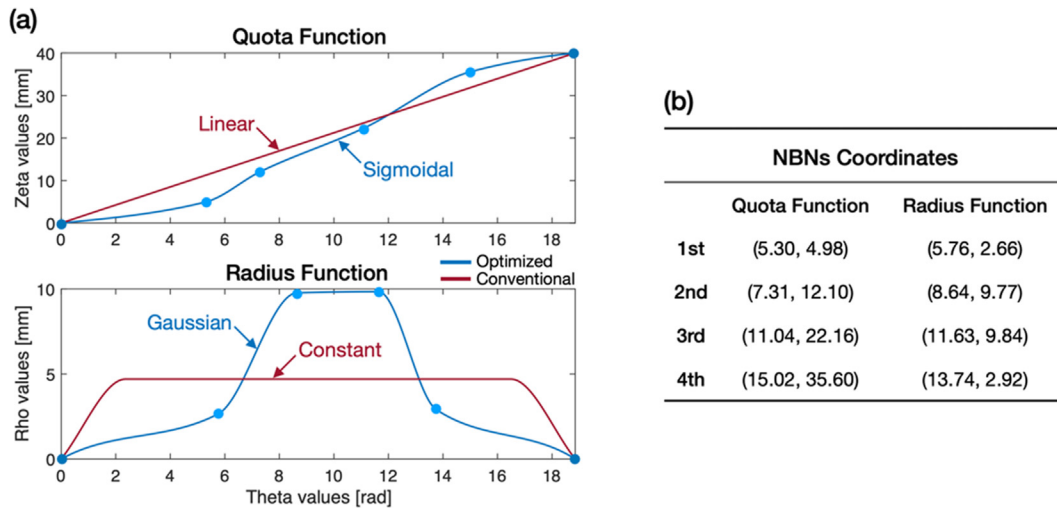


Fig. B1. Results from GA optimization process. (a) Quota and radius functions for optimized and conventional three coils geometries, (b) correspondent NBNS coordinates.

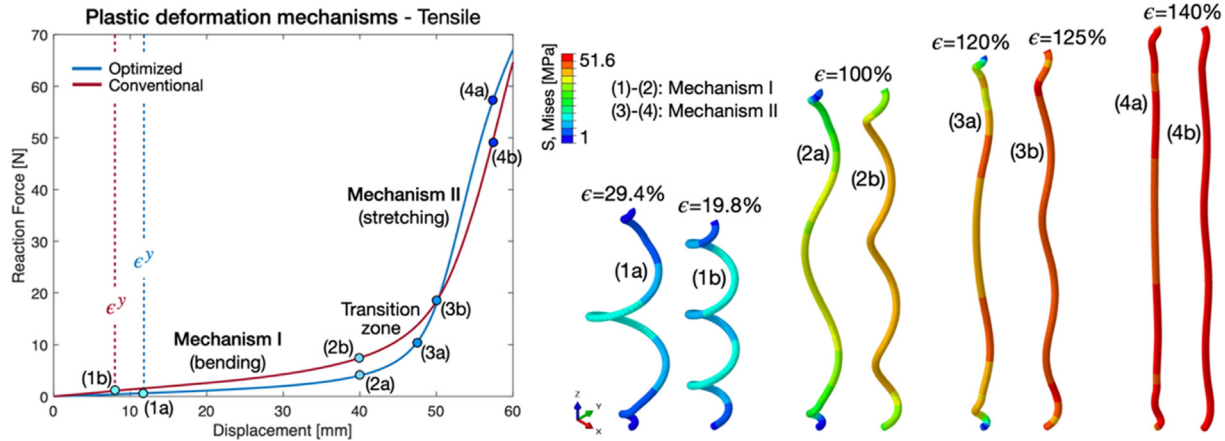


Fig. C1. Reaction force vs tensile displacement curves and plastic deformation mechanisms involved for three coils geometries.

Appendix D

See Table D1, Table D2, Table D3

Table D1 Poly(lactic Acid (PLA) elastic material properties and plastic stress–strain data [23].

Mechanical properties	
Density $\rho$	1250 kg/m <sup>3</sup>
Elastic material properties	
Elastic Modulus $E$	1700 MPa
Yield Stress $\sigma^y$	22.0 MPa
Ultimate Stress $\sigma^u$	43.5 MPa
Poisson's Ratio $\nu$	0.36
Plastic material properties	
Plastic Stress [MPa]	Plastic Strain [mm/mm]
22.0,22.2,25.7,29.5,33.0,36.6,40.1,43.5	0.0,0.016,0.02,0.025,0.03,0.035,0.04,0.045

Table D2 Johnson-Cook plasticity constants for Aluminum 70–75 T6 [31].

Physical properties	
Density $\rho$	2810 kg/m <sup>3</sup>
Elastic material properties	
Elastic Modulus $E$	71.7 GPa
Yield Stress $\sigma^y$	473 MPa
Poisson's Ratio $\nu$	0.33
Johnson-Cook plastic properties	
$A, B, n$	473 MPa, .210 MPa, .0.3813

Table D3 Ogden material parameters ( $n = 3$ ) for Ethylene-Propylene Diene Monomer EPDM [37].

$i$	$\mu_i$	$\alpha_i$
1	0.994929240	3.36255675
2	0.060157293	9.76206145
3	0.077564639	-4.61426912

Appendix E

See Fig. E1

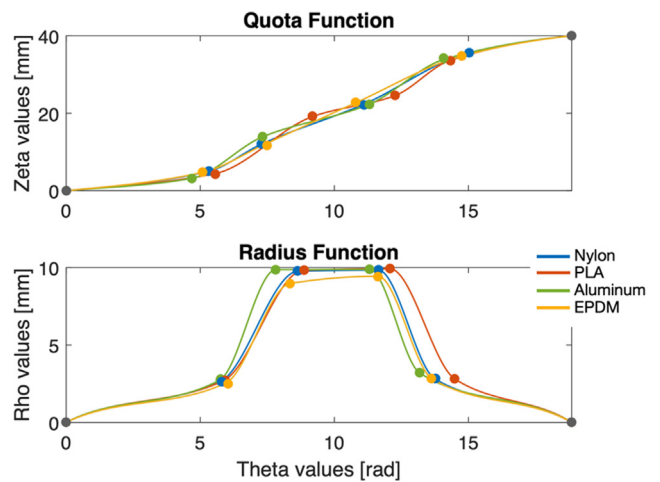


Fig. E1. Results from GA optimization process showing quota and radius functions for optimized three coils geometries for varying material properties.

## References

- [1] W.H. Wittrick, On elastic wave propagation in helical springs, *Int. J. Mech. Sci.* 8 (1) (1966) 25–47.
- [2] J.E. Mottershead, Finite elements for dynamical analysis of helical rods, *Int. J. Mech. Sci.* 22 (5) (1980) 267–283.
- [3] M. Taktak, F. Dammak, S. Abid, M. Haddar, A mixed-hybrid finite element for three-dimensional isotropic helical beam analysis, *Int. J. Mech. Sci.* 47 (2) (2015) 209–229.
- [4] Z. Zhang, Z. Qi, Z. Wu, H. Fang, A spatial Euler-Bernoulli beam element for rigid-flexible coupling dynamic analysis of flexible structures, *Shock Vib.* (2015).
- [5] C. Meier, A. Popp, W.A. Wall, An objective 3D large deformation finite element formulation for geometrically exact curved Kirchhoff rods, *Computat. Meth. Appl. Mech. Eng.* 278 (2014) 445–478.
- [6] A.N. Chaudhury, D. Datta, Analysis of prismatic springs of non-circular coil shape and non-prismatic springs of circular coil shape by analytical and finite element methods, *J. Comput. Des. Eng.* 4 (3) (2017) 178–191.
- [7] J. Zhang, Z. Qi, G. Wang, S. Guo, High-Efficiency Dynamic Modeling of a Helical Spring Element Based on the Geometrically Exact Beam Theory, *Shock Vib.* (2020).
- [8] L.E. Becker, W.L. Cleghorn, On the buckling of helical compression springs, *Int. J. Mech. Sci.* 34 (4) (1992) 275–282.
- [9] F. De Crescenzo, P. Salvini, Two-Dimensional Discrete Model for Buckling of Helical Springs, *Proceedings of AIAS 2019 International Conference on Stress Analysis*, 2019.
- [10] V. Yildirim, Numerical buckling analysis of cylindrical helical coil springs in a dynamic manner, *Int. J. Eng. Appl. Sci.* 1 (2009) 20–32.
- [11] C. Zhou, M.R. Chi, Z.F. Wen, X.W. Wu, An investigation of abnormal vibration-induced coil spring failure in metro vehicles, *Eng. Fail. Anal.* 108 (2020).
- [12] W. Sun, D. Thompson, J. Zhou, The influence of vehicle-track dynamic coupling on the fatigue failure of coil springs within the primary suspension of metro vehicles, *Veh. Syst. Dyn.* 12 (2019) 1–17.
- [13] L. Dai, M. Chi, H. Gao, J. Sun, An Investigation into the Modeling Methodology of the Coil Spring, *Shock Vib.* (2020).
- [14] D. Kumar, L.H. Poh, S.T. Quek, Isogeometric shape optimization of missing rib auxetics with prescribed negative Poisson's ratio over large strains using genetic algorithm, *Int. J. Mech. Sci.* 193 (2021).
- [15] Yokota, T., Taguchi, T. and Gen, M. (1997) "A solution method for optimal weight design problem of helical spring using genetic algorithms", *Proceedings of the 21st International Conference in Computational Industrial Engineering*, 33 (1–2), pp. 71–76.
- [16] Q. Xiao, L. Liu, Q. Xiao, The optimal design and simulation of helical spring based on particle swarm optimization algorithm and MATLAB, *Wseas Transactions on Circuits and Systems* 8 (1) (2009) 84–93.
- [17] M. Taktak, K. Omheni, A. Aloui, Dynamic optimisation design of a cylindrical helical spring, *Appl. Acoust.* 77 (2014) 178–183.
- [18] B.W. Zhan, L.Y. Sun, B.C. Huang, Design and optimisation of automotive composite helical spring, *J. Beijing Univ. Aeronaut. Astronautics* 44 (7) (2018) 1520–1527.
- [19] O. Zebdi, R. Boukhili, F. Trochu, Optimum design of a composite helical spring by Multi-criteria Optimisation, *J. Reinforced Plastic Compos.* 28 (14) (2009) 1713–1732.
- [20] F. Ratle, B. Lecarpentier, R. Labib, Multi-objective optimisation of a composite material spring design using an evolutionary algorithm, Heidelberg, *Parallel Problem Solving from Nature - PPSN VIII*, Springer, Berlin, 2004.
- [21] J.B. Bai et al., Determining the best practice - Optimal designs of composite helical structures using Genetic Algorithms, *Compos. Struct.* 221 (2021).
- [22] J. Lim, C. You, I. Dayyani, Multi-objective topology optimization and structural analysis of periodic spaceframe structures, *Mater. Des.* 190 (2020).
- [23] A. Jha, I. Dayyani, Shape optimisation and buckling analysis of large strain zero Poisson's ratio fish-cells metamaterial for morphing structures, *Compos. Struct.* 268 (2021).
- [24] A. Ermakova, I. Dayyani, Shape optimisation of composite corrugated morphing skins, *Compos. B Eng.* 115 (2017) 87–101.
- [25] X.S. Yang, Nature-inspired optimization algorithms: Challenges and open problems, *J. Comput. Sci.* 46 (2020).
- [26] Mathworks Inc., 2020, Genetic Algorithm Options, MATLAB documentation (R2020B), Available at: <https://it.mathworks.com/help/gads/genetic-algorithm-options.html> (accessed 1 July 2021).
- [27] I. Dayyani, M.I. Friswell, Multi-objective optimization for the geometry of trapezoidal corrugated morphing skins, *Struct. Multidisciplinary Optimizat.* 55 (2017) 331–345.
- [28] Mathworks Inc., 2020, gamultiobj Algorithm, MATLAB documentation (R2020B), Available at: <https://it.mathworks.com/help/gads/gamultiobj-algorithm.html> (accessed 1 July 2021).
- [29] M. Naghavi Zadeh, I. Dayyani, M. Yasaee, Fish cells, a new zero Poisson's ratio metamaterial - Part I: design and experiment, *J. Intell. Mater. Syst. Struct.* 31 (2020) 1617–1637.
- [30] R.T. Marler, J.S. Arora, Survey of multi-objective optimization methods for engineering, *Struct. Multidisciplinary Optimizat.* 26 (2004) 369–395.
- [31] D.N. Zhang, Q.Q. Shanguan, C.J. Xie, F. Liu, A modified Johnson-Cook model of dynamic tensile behaviors for 7075-T6 aluminum alloy, *J. Alloy. Compd.* 619 (2015) 186–194.
- [32] ASTM International, *Standard Test Method for Tensile Properties of Plastics* (ASTM D838-14), 2014.
- [33] Z. Vangelatos et al., Strength through defects: A novel Bayesian approach for the optimization of architected materials, *Sci. Adv.* 7 (2021).
- [34] Z. Vangelatos, K. Komvopoulos, C.P. Grigoropoulos, Regulating the mechanical behavior of metamaterial microlattices by tactical structure modification, *J. Mech. Phys. Solids* 144 (2020).
- [35] Z. Vangelatos, X.G. Gu, C.P. Grigoropoulos, Architected metamaterials with tailored 3D buckling mechanisms at the microscale, *Extreme Mech. Lett.* 33 (2019).
- [36] Z. Vangelatos, K. Komvopoulos, C.P. Grigoropoulos, Vacancies for controlling the behavior of microstructured three-dimensional mechanical metamaterials, *Mathematics Mech. of Solids* 24 (2) (2019) 511–524.
- [37] C. Feichter, Z. Major, R.W. Lang, Deformation analysis of notched rubber specimens, *Strain* 42 (4) (2006) 299–304.